

The Low-Frequency Solar Corona in Circular Polarization

Patrick I. McCauley¹  · Iver H. Cairns¹  ·
Stephen M. White²  · Surajit Mondal³ · Emil Lenc⁴  ·
John Morgan⁵ · Divya Oberoi³ 

© Springer ●●●●

Abstract

We present spectropolarimetric imaging observations of the solar corona at low frequencies (80–240 MHz) using the *Murchison Widefield Array* (MWA). These images are the first of their kind, and we introduce an algorithm to mitigate an instrumental artefact by which the total intensity signal contaminates the polarimetric images due to calibration errors. We then survey the range of circular polarization (Stokes V) features detected in over 100 observing runs near solar maximum during quiescent periods. First, we detect around 700 compact polarized sources across our dataset with polarization fractions ranging from less than 0.5 % to nearly 100 %. These sources exhibit a positive correlation between polarization fraction and total intensity, and we interpret them as a continuum of plasma emission noise storm (Type I burst) continua sources associated with active regions. Second, we report a characteristic “bullseye” structure observed for many low-latitude coronal holes in which a central polarized component is surrounded by a ring of the opposite sense. The central component does not match the sign expected from thermal bremsstrahlung emission, and we speculate that propagation effects or an alternative emission mechanism may be responsible. Third, we show that the large-scale polarimetric structure at our lowest frequencies is reasonably well-correlated with the line-of-sight (LOS) magnetic field component inferred from a global potential field source surface (PFSS) model. The boundaries between opposite circular polarization signs are generally aligned with polarity inversion lines in the model at a height roughly corresponding to that of the radio limb. This is not true at our highest frequencies, however, where the LOS magnetic field direction and polarization sign are often not straightforwardly correlated.

✉ P. I. McCauley
patrick.mccauley@sydney.edu.au

¹ School of Physics, University of Sydney, Sydney, NSW 2006, Australia

² Space Vehicles Directorate, Air Force Research Laboratory, Albuquerque, NM, USA

³ National Centre for Radio Astrophysics, Ganeshkind, Pune 411007, Maharashtra, India

⁴ CSIRO Astronomy and Space Science, PO Box 76, Epping, NSW 1710, Australia

⁵ International Centre for Radio Astronomy Research, Curtin University, Perth, WA 6845, Australia

Keywords: Polarization, Radio; Corona, Radio Emission; Magnetic fields, Corona; Coronal Holes; Radio Bursts, Type I; Radio Emission, Active Regions; Radio Emission, Quiet; Instrumental Effects; Spectropolarimetry

1. Introduction

Radio emission in a magnetized plasma is produced in one or both of two modes, the ordinary [o] and extraordinary [x], which are each 100 % circularly polarized with opposite senses in the quasi-circular approximation generally used for the solar corona (Zheleznyakov, 1977; Melrose, 1980). The x -mode refers to when the electric field vector of the electromagnetic wave rotates in the same direction as the gyromotion of electrons around the magnetic field where the emission was generated. A net circular polarization arises when the two modes are received unequally, which is characterized by the degree [r_c] of circular polarization [Stokes V] relative to the total intensity [Stokes I]. In detail,

$$r_c = \frac{T_{b,x} - T_{b,o}}{T_{b,x} + T_{b,o}}, \quad (1)$$

where $T_{b,x}$ and $T_{b,o}$ refer to the brightness temperatures of the o and x modes, respectively (Dulk, 1985). The quantity r_c , also labeled dcp or V/I , depends on the emission mechanism and plasma parameters, along with a number of effects such as mode coupling and refraction that may modulate the polarization state or separate the two modes during propagation. Low-frequency (meter-wave) emission from the solar corona is dominated by two mechanisms, thermal bremsstrahlung and plasma emission (*e.g.* Dulk, 1985; White, 1999; Aschwanden, 2005). Other mechanisms are also important in specific contexts, such as (gyro)synchrotron emission in coronal mass ejections, but these will not be discussed in detail here.

Bremsstrahlung emission is produced by the conversion of kinetic energy into radiant energy that occurs when a charged particle accelerates, and thermal bremsstrahlung refers to a plasma in thermal equilibrium for which free electrons are deflected by the Coulomb fields of ions and atomic nuclei. This is often referred to as free-free radiation for a fully-ionized plasma like the corona because the particles are not in bound states throughout the entire process. Emission at a particular frequency is generated only by plasma with electron densities [n_e] equal to or below that corresponding to the local fundamental electron plasma frequency [$f_p \approx 9 \times 10^{-3} \sqrt{n_e}$ MHz, for n_e in cm^{-3}]. Lower-frequency emission therefore corresponds to lower-density material at generally larger heights above the surface, meaning that the corona appears larger with decreasing frequency. Canonical coronal background density models (*e.g.* Newkirk, 1961; Saito, Poland, and Munro, 1977) correspond to frequencies of below ≈ 300 MHz, but dense coronal structures may produce free-free emission well into the GHz range.

Thermal bremsstrahlung slightly favors the x -mode to a degree that depends primarily on the line-of-sight (LOS) magnetic field strength. The opacity, κ , can be written as

$$\kappa = 0.2 \frac{n_e^2}{T_e^{1.5} (f \pm f_B |\cos \theta|)^2} \text{ cm}^{-1}, \quad (2)$$

where T_e is the electron temperature, f is the emission frequency, f_B is the electron gyrofrequency [$f_B = 2.8 \times 10^6 B_{\text{gauss}}$ Hz], and θ is the angle between the line of sight

and the magnetic field direction (Dulk, 1985; Gelfreikh, 2004; Gibson *et al.*, 2016). The plus sign refers to the *o*-mode, the minus sign refers to the *x*-mode, and the difference between the two modes produces the net circular polarization. Equation 2 is a quasi-linear (QL) approximation that is valid for most angles θ . Values of θ close to 90° , for which the propagation direction is nearly perpendicular to the magnetic field orientation, are referred to as quasi-transverse (QT) propagation and produce linear polarizations (Zheleznyakov, 1970; Ryabov, 2004). Circularly-polarized emission that passes through a QT region may also experience polarization state changes, which will be discussed in Section 7. Equation 2 also assumes that $f \gg f_B$. This condition means that the difference between the two modes, and therefore the polarization fraction, will always be fairly small, generally a few percent or less at the low frequencies considered in this article (Sastry, 2009). For a homogenous, optically-thin plasma, $r_c \approx 2 \cos \theta (f_B/f)$, while for the optically-thick case, a temperature gradient is required for the two modes to be produced unequally (Dulk, 1985; Gibson *et al.*, 2016).

Thermal bremsstrahlung radiation generates a continuous background that slowly varies as the corona evolves. This may be slightly or dramatically augmented by transient emission associated with nonthermal electrons that are accelerated through a variety of mechanisms underpinned either by magnetic reconnection or shock waves. These electron streams produce oscillations in the background plasma known as Langmuir waves, which then deposit energy into radio emission through scattering by ion sound waves or by other nonlinear Langmuir wave processes (Ginzburg and Zhelezniakov, 1958; Robinson and Cairns, 2000; Melrose, 2009). These are typically coherent mechanisms, often grouped together under the term “plasma emission,” for which the intensity is related nonlinearly to the energy of the nonthermal electrons. Plasma emission is responsible for most types of solar radio bursts (Dulk, 1985), which may exceed the thermal background by several orders of magnitude, but it is also likely the source of very weak nonthermal emissions that enhance the background only slightly (Suresh *et al.*, 2017; Sharma, Oberoi, and Arjunwadkar, 2018). Like thermal bremsstrahlung, plasma emission is tied to the ambient density though the electron plasma frequency. However, in this case, the emission frequency is highly localized to just above the plasma frequency or its harmonic.

The polarization of plasma emission depends firstly on the harmonic number. For fundamental [f_p] emission, the circular polarization fraction should be 100 % in the sense of the *o*-mode because, for frequencies expressed in Hz, f_p is above the cutoff for *x*-mode production, meaning that *x*-mode radiation begins only at frequencies slightly lower than the plasma frequency (Melrose, 2009). Polarization fractions approaching 100 % are indeed sometimes observed for Type I bursts (*e.g.* Kai, 1962; Tsuchiya, 1963; Dulk, Suzuki, and Sheridan, 1984; Aschwanden, 1986; Mugundhan *et al.*, 2018). However, this is almost never true for other radio burst types that are also attributed to fundamental plasma emission (*e.g.* Wentzel, 1984; Reid and Ratcliffe, 2014; Kaneda *et al.*, 2015). The reason for this remains an open question, but a common explanation is that scattering of the radio emission by other wave modes or by sharp density gradients tends to have a depolarizing effect (*e.g.* Wentzel, Zlobec, and Messerotti, 1986; Melrose, 1989, 2006; Kaneda *et al.*, 2017). The polarization fraction of harmonic [$2f_p$] emission is more complicated because it depends on the angular distribution of the Langmuir waves. Polarization in the sense of the *o*-mode is still generally expected, assuming that the Langmuir waves are confined to relatively small angles with respect to the magnetic field, which is generally assumed to be true because of the associated magnetic field strengths (Melrose, Dulk, and Smerd, 1978). However, it is possible for the *x*-mode to dominate in specific, and likely less common,

contexts (Willes and Melrose, 1997). Thus, for the same LOS magnetic field direction, the two dominant low-frequency emission mechanisms generally produce opposite circular polarization signatures.

Radio polarimetry has long been a powerful tool for diagnosing solar magnetic fields, particularly using high-frequency observations of gyroresonance emission (Akhmedov *et al.*, 1982; White and Kundu, 1997) and, more recently, bremsstrahlung emission (Grebinskij *et al.*, 2000). Low-frequency polarimetry has generally been restricted to radio bursts because their high intensities and large polarization fractions are easiest to detect. An early review on the polarization of metric bursts and their utility as magnetic field probes is given by Dulk and McLean (1978). Very few instruments have been capable of making two-dimensional polarimetric measurements of the low-frequency Sun, and until now, none have been sensitive enough to detect the weak polarization signatures during quiescent periods. In recent decades, this type of analysis could be done with two instruments, the Nançay Radioheliograph (NRH; Kerdraon and Delouis, 1997), which operates between 150 and 450 MHz, and the Gauribidanur Radioheliograph (GRH; Ramesh *et al.*, 1998), which usually operates at 80 MHz.

A few studies have utilized the polarimetric imaging capabilities of the NRH to examine spatial variation in radio bursts. For example, Mercier (1990) showed that Type III bursts have different spatial characteristics in circular polarization compared to the total intensity, and Bouratzis *et al.* (2016) investigated similar differences in spike bursts as a function of time. Several others have examined source positions and structures in total intensity NRH observations, while using the polarization information to help discriminate between emission mechanisms (*e.g.* Gopalswamy *et al.*, 1994; Tun and Vourlidas, 2013; Kong *et al.*, 2016; Liu *et al.*, 2018). The radioheliograph at Gauribidanur does not have a polarimetric capability itself, but several one-dimensional polarimeters have been installed alongside it (Ramesh *et al.*, 2008; Sasikumar Raja *et al.*, 2013; Kishore *et al.*, 2015).

GRH imaging and simultaneous polarimeter observations have been used for studies of Type I noise storms (Ramesh, Kathiravan, and Narayanan, 2011; Ramesh *et al.*, 2013; Mugundhan *et al.*, 2018), Type II bursts (Hariharan *et al.*, 2014; Hariharan, Ramesh, and Kathiravan, 2015; Kumari *et al.*, 2017), Type III bursts (Ramesh *et al.*, 2010; Sasikumar Raja and Ramesh, 2013; Kishore *et al.*, 2017), Type IV bursts (Hariharan *et al.*, 2016), and gyrosynchrotron emission from CMEs (Sasikumar Raja *et al.*, 2014). Most of these results include estimates of the associated magnetic field strength assuming a particular emission mechanism. Additionally, Ramesh, Kathiravan, and Sastry (2010) report polarized emission from streamers that is attributed to thermal bremsstrahlung, though the polarization fraction ($\approx 15\%$) is unusually large for bremsstrahlung emission. Moreover, the polarized source cannot be localized beyond assuming that it comes from the dominant total intensity source, and as we will show, polarized emission from the low-frequency corona is often not straightforwardly correlated with total intensity, particularly during quiescent periods.

This article presents the first spectropolarimetric imaging observations of the Sun from the *Murchison Widefield Array* (MWA; Tingay *et al.*, 2013). These are the first circular polarization images of the low-frequency corona that are sensitive enough to detect the polarimetric signatures associated with thermal bremsstrahlung emission and very weak plasma emission outside of major burst periods. We will survey the range of features detected in over 100 observing runs near solar maximum and motivate future studies with these novel data. Section 2 describes the MWA instrument, and Section 3 introduces an algorithm used to mitigate an important calibration artefact. Section 4 discusses active region noise storm sources, Section 5 characterizes the polarimetric signature of coronal

holes, and Section 6 details the large-scale quiescent structure. We discuss the implications of our results and motivate future studies in Section 7. Our conclusions are summarized in Section 8.

2. Murchison Widefield Array (MWA)

The MWA is a low-frequency radio interferometer located in Western Australia (Lonsdale *et al.*, 2009; Tingay *et al.*, 2013), and heliophysics is among the instrument’s principal science themes alongside astrophysical topics (Bowman *et al.*, 2013). Direct solar observations have characterized the weakest nonthermal emissions reported to-date (Suresh *et al.*, 2017; Sharma, Oberoi, and Arjunwadkar, 2018), provided definitive evidence for the standard theory of Type III bursts (Cairns *et al.*, 2018), detailed new radio burst dynamics (McCauley *et al.*, 2017; Mohan *et al.*, 2018), used radio bursts to probe the coronal density structure (McCauley, Cairns, and Morgan, 2018), characterized the low-frequency signature of coronal holes (Rahman, McCauley, and Cairns, 2019), and provided evidence for coronal heating via weak particle acceleration episodes (Mohan *et al.*, 2019). Solar imaging with the MWA has also motivated advances in data processing techniques related to flux calibration (Oberoi, Sharma, and Rogers, 2017), spatially resolved dynamic spectra (Mohan and Oberoi, 2017), and high dynamic range imaging (Mondal *et al.*, 2019). Additionally, widefield interplanetary scintillation observations may be used for studies of the solar wind and of coronal mass ejections (CMEs) propagating through the heliosphere (Kaplan *et al.*, 2015; Morgan *et al.*, 2018).

The MWA is comprised of 4096 dipole antennas arranged in 128 aperture arrays called “tiles”. This refers to the Phase I array used here, which began observing in 2013. An expanded Phase II array began full operations in 2018 with twice as many tiles, of which 128 can be used simultaneously in different configurations (Wayth *et al.*, 2018). The MWA has an instantaneous bandwidth of 30.72 MHz that can be distributed between 80 and 300 MHz in various configurations. Our data utilize a “picket fence” mode with 12 contiguous 2.56 MHz bandwidths centered at 80, 89, 98, 108, 120, 132, 145, 161, 179, 196, 217, and 240 MHz. The data were recorded with a 0.5 sec time resolution and a 40 kHz spectral resolution, but the observations presented here are averaged over each 2.56 MHz bandwidth before imaging and then time-averaged to different degrees after imaging. The spatial resolution is defined by the synthesized beam sizes, which have major axes of around 6.4 arcmin ($0.40 R_{\odot}$) at 80 MHz and 2.5 arcmin ($0.16 R_{\odot}$) at 240 MHz. The beam sizes and orientations, shown in the lower-left corners of each image, vary somewhat between observations due to pointing differences and occasional antenna failures.

We use the same data processing scheme as McCauley *et al.* (2017) and McCauley, Cairns, and Morgan (2018), and what follows is a brief summary thereof. Visibilities were generated with the standard MWA correlator (Ord *et al.*, 2015) and the cotter software (Offringa, van de Gronde, and Roerdink, 2012; Offringa *et al.*, 2015). Observations of bright and well-modelled calibrator sources were used to obtain solutions for the complex antenna gains (Hurley-Walker *et al.*, 2014), which were improved by imaging the calibrator and iteratively self-calibrating from there (Hurley-Walker *et al.*, 2017). All of our observations were calibrated using either Centaurus A or Hercules A. WSClean (Offringa *et al.*, 2014) was used to perform the imaging with a Briggs -2 weighting (Briggs, 1995) to emphasize spatial resolution and minimize point spread function (PSF) sidelobes. The primary beam model of Sutinjo *et al.* (2015) was used to produce Stokes I and V images from the instrumental polarizations, and the SolarSoftWare (SSW; Freeland and Handy, 1998) routine `mwa_prep`

(McCauley *et al.*, 2017) was used to translate the images onto solar coordinates. The data presented here are not flux calibrated on an absolute scale. Intensities are expressed either relative to the Stokes I background level or in units of signal-to-noise.

The next section will describe further steps required to calibrate the polarization images. We use the International Astronomical Union (IAU) and Institute of Electrical and Electronics Engineers (IEEE) convention on circular polarization, which defines positive as being right-handed (clockwise) from the source’s perspective (IEEE, 1969; IAU, 1973), where right-handed refers to the rotation of the electric field vector of the electromagnetic wave about the orthogonal direction of motion. This convention is convenient here because it means that a net polarization in the sense of the x -mode will match the sign of the line-of-sight magnetic field component [B_{LOS}], where positive is outward.

Each observation period lasted around 5 minutes, and a total of 111 such periods in 2014 and 2015 were reduced. 52 of these were imaged at the full 0.5-sec time resolution and 59 were sampled at a 4-sec cadence. Our objective is to survey the longer-lived features that are present in the corona on timescales of at least minutes, outside of transient radio burst periods. All of the images presented in this article are median averages of the individual 0.5-sec integrations with total intensities that are within two standard deviations of the background level during each 5-min observing window. Depending on the sources present, these averaged background images may still contain significant nonthermal emission. Identifying which images to include in the average is done automatically using the baseline procedure illustrated by Figure 5 of McCauley, Cairns, and Morgan (2018). This involves finding the total intensity in each image, excluding times for which the intensity is greater than two standard deviations above the median, and iterating until no more images are excluded. Each pixel in the output image then contains the median of the corresponding pixels in those low-intensity images. The consideration of time dependent behavior on scales of less than 5 minutes will be a topic of future work.

3. An Algorithm to Mitigate the Leakage of Stokes I into V

To obtain useful polarimetric images, it is necessary to account for possible “leakage” of the Stokes I signal into the other Stokes parameters. The MWA uses dual-polarization dipole antennas arranged in 4×4 grids, or “tiles”, where the signals for each tile component are combined in an analog beamformer that produces two outputs representing orthogonal X and Y linear polarizations (Tingay *et al.*, 2013). The beamformer outputs are correlated into products that fully describe the polarization state in “instrumental” polarizations (XX , YY , XY , and YX) that may be converted into the standard Stokes parameters (I , Q , U , and V) using a model of the MWA beam pattern. However, there are significant differences between the analytic beam pattern and that measured empirically by imaging known sources (Sutinjo *et al.*, 2015). These differences between the actual instrumental response and the complex primary beam model lead to “leakage” errors in the Stokes images where some fraction of I contaminates the other parameters.

A more detailed description of this problem and of MWA polarimetry in general is given by Lenc *et al.* (2017). Sources of discrepancy between the beam model and the true response include imperfections in the model itself along with instrumental effects, such as individual dipole failures during a particular observing run, that may cause the true response to vary from an otherwise perfect beam model. Importantly, the polarimetric response is also affected by a source’s position within the beam and zenith angle, which means that the response changes somewhat between the observation used to calibrate the

array and the solar observation. Changes in the ionosphere over the $\lesssim 5$ hours between the calibrator and solar observations may also degrade the calibration solution. Our data were reduced using the Sutinjo *et al.* (2015) beam model, which dramatically reduced leakage from Stokes I into Stokes Q but somewhat increased the leakage from I into V compared to previous beam models.

The leakage fraction also varies with a source’s position on the sky and its position within the field-of-view for a given calibration solution (Sutinjo *et al.*, 2015; Lenc *et al.*, 2017, 2018). Sources observed at lower elevations and/or near the edge of the field tend to exhibit higher leakage fractions. It is possible to reduce the leakage by means of iterative self-calibration on the source of interest, but this may affect the polarimetric calibration in ways that are difficult to understand, and self-calibration can also be difficult to effectively apply to diffuse sources like the Sun. Instead, the leakage effect can be mitigated with an empirical correction if there are sources within the field for which the polarization fractions are known. For the very large fields typical of many astrophysical MWA observations, a two-dimensional fit to the leakage fraction may be obtained from the known sources scattered throughout the field. The leakage fraction may vary by as much as 8 % across a 25 deg² patch (Lenc *et al.*, 2017), but we do not expect significant variations across the spatial extent of the radio Sun ($\lesssim 1.2^\circ$ at 80 MHz) or over the duration of a typical observation (≈ 5 min).

For the solar observations presented here, it is not possible to simultaneously observe background sources alongside the Sun due to limited dynamic range. Recent advances in calibration techniques may enable this capability (Mondal *et al.*, 2019), but those methods cannot yet be used for polarimetry and are not used here. In other words, the astronomical sources that may be present are too faint to be observed in close proximity to the Sun and cannot be used to characterize the Stokes I into V leakage. We also do not know what the polarization fraction of any particular region on the Sun should be at any given time, as the polarization fraction may vary considerably depending on the dominant emission mechanism and local plasma parameters. However, outside of radio bursts, solar emission at low frequencies is dominated by the thermal bremsstrahlung (free-free) process. The importance of this is that under normal quiet-Sun conditions at MWA wavelengths, we can expect to see bremsstrahlung radiation in most locations that is only slightly polarized, and we can use this statistical information to estimate the leakage fraction with an algorithm that minimizes the number of pixels with polarization fractions greater than some threshold (*i.e.* $|V/I| > r_{c,\text{thresh}}$).

To determine this threshold, we generated synthetic Stokes V/I images for each of our observing periods and frequencies using the forward modeling code FORWARD (Gibson *et al.*, 2016) in SolarSoft IDL. FORWARD calculates the Stokes I and V intensities expected from thermal bremsstrahlung emission using Equation 2, with the temperature, density, and magnetic field parameters taken in this case from the month-averaged Magnetohydrodynamic Algorithm outside a Sphere (MAS; Lionello, Linker, and Mikić, 2009) global coronal model. On average 50 % of pixels in these images with Stokes I brightness temperatures greater than 100,000 K have fractional polarizations of less than 0.3 %. We choose a slightly larger threshold of 0.5 % because we wanted to implement our procedure uniformly, and the noise level in some of our observations makes a lower threshold impractical. This value is also consistent with the predictions of Sastry (2009), and the effect of varying the threshold is folded into V/I uncertainty estimates presented in Section 5.

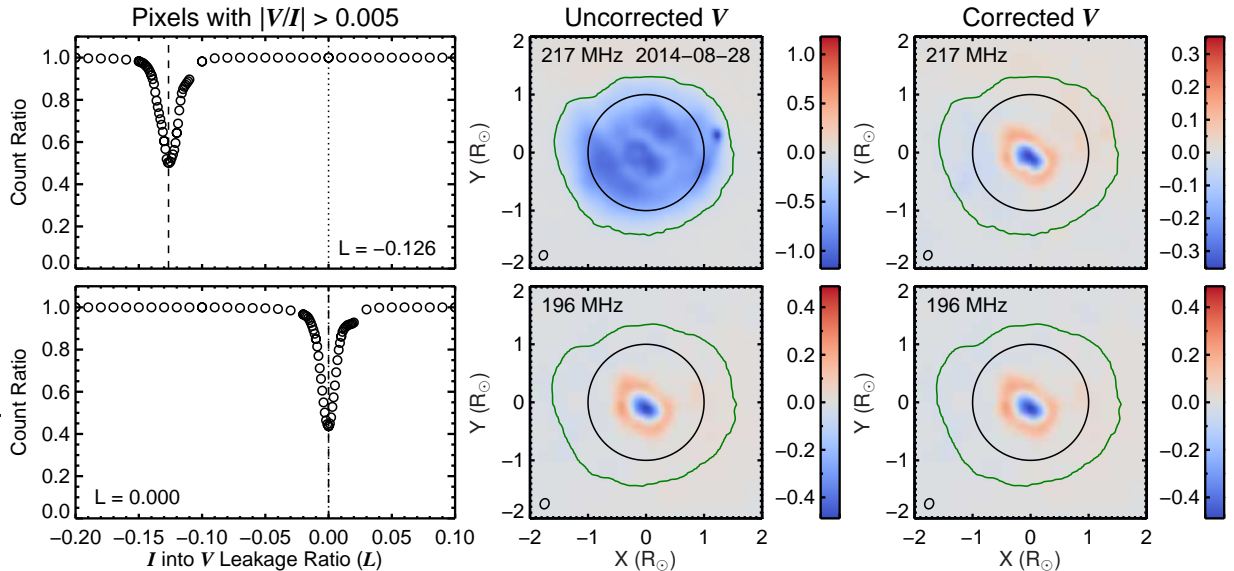


Figure 1. An illustration of the leakage subtraction algorithm. The left panels show the implementation of Equation 4 to find the L that minimizes the number of pixels with $|V/I| > 0.005$. At 217 MHz (top), we estimate that -12.5 % of the Stokes I signal leaked into Stokes V , and at 196 MHz, the same procedure estimates there to be no leakage. The middle panels show the uncorrected Stokes V images, and the right panels show the corrected images (*i.e.* $V - L \cdot I$). The corrected image at 217 MHz is shown as a function of L in an animated version of this figure available in the [online material](#).

Our algorithm therefore assumes that most of the pixels in our images of the quiescent corona should exhibit polarization fractions of less than 0.5 % and determines the leakage fraction that minimizes the number of pixels with V/I values greater than 0.005. The algorithm can be expressed formally as:

$$f(L) = \sum_{k=1}^n \left[\left| \frac{V_k - L \cdot I_k}{I_k} \right| > r_{c,\text{thresh}} \right] \quad (3)$$

$$L_{\min} = \arg \min_{L \in (-1,1)} f(L), \quad (4)$$

where $f(L)$ is the number of pixels with polarization fractions greater than $r_{c,\text{thresh}}$ as a function of L , the constant fraction of Stokes I that is assumed to have leaked into Stokes V . The aim is to find the value L_{\min} that minimizes $f(L)$, where k is a given pixel in an image and n is the number of pixels to be considered. We consider only pixels for which a Stokes I signal is detected above 5σ . The square brackets in Equation 3 refer to the Iverson bracket notation, meaning that their contents evaluate to 1 if the condition is satisfied and 0 otherwise. In this case, that simply means that a pixel is counted if its polarization fraction is greater than 0.005 (0.5 %). Equation 4 is evaluated using an adaptive grid search with increments in L of 0.1, 0.01, and 0.001. Note that this strategy is not the same as minimizing the total polarized intensity, which is not advisable because the two senses may not be equally represented and specific regions may have large polarized intensities that would bias the result if one were to simply find L that minimizes the total polarization fraction in the image.

Figures 1 and 2 show the result of applying this algorithm to images from two frequency channels on two different days. In Figure 1, we see that the uncorrected Stokes V image

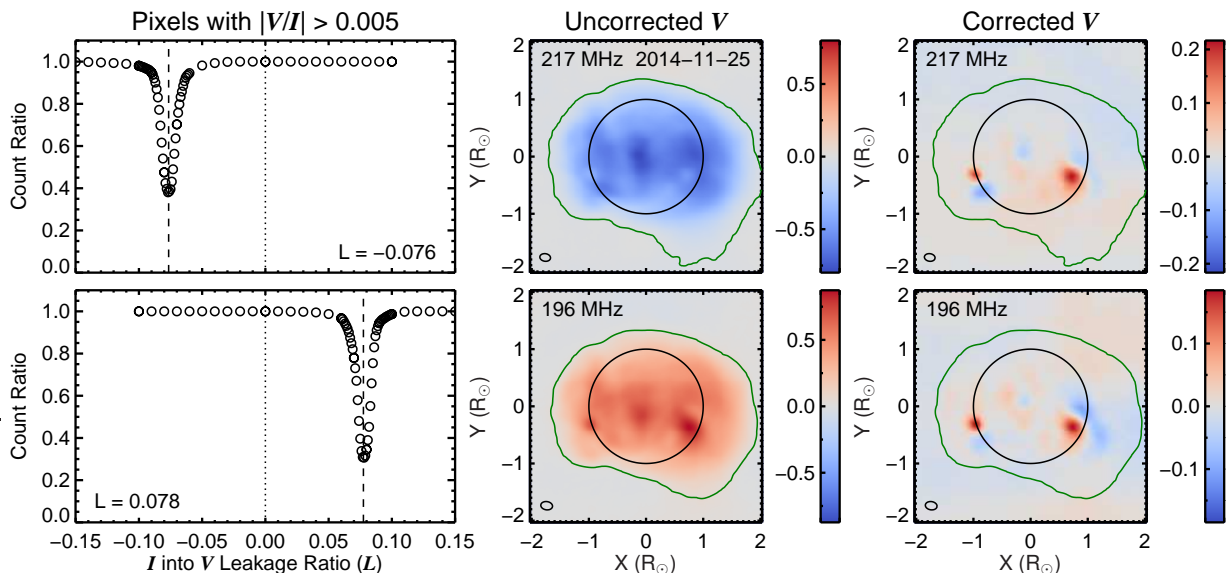


Figure 2. Same as Figure 1 but for a different observation with different structures and a different leakage behavior.

at 217 MHz would imply that the entire corona is highly circularly polarized with a single sense, while the uncorrected 196 MHz image suggests a very different structure with a mixture of opposite signs. We know that entire corona at 217 MHz should not be polarized with a single sense to the extent implied by the uncorrected 217 MHz image. Our algorithm suggests that $L = -0.125$ in this case, and applying that correction recovers the same structure that is apparent in the 196 MHz image. Importantly, the same procedure can also be applied to observations for which there is little or no leakage, as is illustrated by the 196 MHz example in Figure 1. Figure 2 shows another example for which the two frequency channels shown are impacted by significant leakage of opposite signs, but once corrected, they exhibit very similar structures.

The examples in Figures 1 and 2 are cases for which the leakage is fairly severe. Figure 3 summarizes the leakage behavior across our dataset. 83 % of the images exhibit leakage fractions less than or equal to 10 %. $L \leq 0.05$ and 0.01 for 66 % and 25 % of the images, respectively. Figure 3d shows that the standard deviation of L is lowest at 179 MHz, which is consistent with the astrophysical MWA literature that indicates the leakage tends to be worst near the ends of the bandwidth. This summary includes 106 different sets of spectroscopic imaging observations for a total of 1144 images to which the algorithm could be applied. In Section 2, we stated that 111 observing periods were analyzed, which would imply 1332 images given our 12 frequency channels. Some images are rejected for polarimetry because they do not contain enough pixels detected above 5σ in Stokes I , generally because a nonthermal active region source is so intense as to elevate the noise floor above the level of the thermal disk. In other words, there is insufficient dynamic range to simultaneously detect both the thermal and nonthermal components present at those times.

These observations must be excluded because the algorithm relies on the statistical expectation that most pixels are dominated by thermal bremsstrahlung emission, and in these cases, there are not enough “thermal” pixels with sufficient signal-to-noise ratios for the algorithm to function. Images were rejected for polarimetry if they contained fewer pixels above 5σ in Stokes I than that enclosed by a circle of radius equal to the height of the plasma frequency layer at a given frequency given a $3\times$ Newkirk (1961) density model,

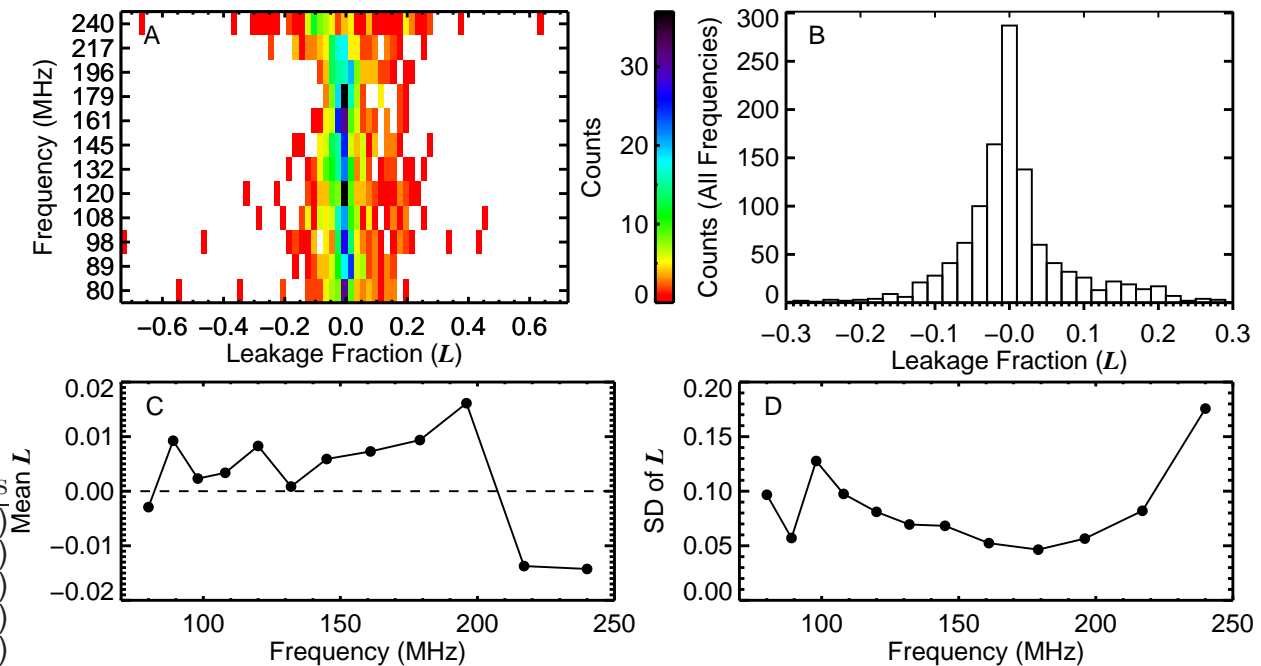


Figure 3. Summary of results from applying the Equation 4 algorithm to 1144 different observations. (A): Two-dimensional histogram showing the leakage fraction [L] as a function of frequency with a bin size of 0.02 in L . (B): Histogram of L across all frequencies. (C): The average L for each frequency channel. (D): The standard deviation of L for each frequency channel. Around 26 % of observations have $|L| < 0.01$, and around 84 % have $|L| < 0.1$. Panels A and D show that the leakage is most severe and variable at the extremes of the bandwidth.

which roughly approximates the height of the radio limb in our observations. Around 14 % of our data failed this test and are excluded from further analysis. It is important to note that this introduces a bias in the next section on active region sources because the most intense sources tend to be the most highly polarized, but the leakage artefact cannot be constrained using our method for the brightest among them. The intense and highly-polarized population is therefore very likely to be underrepresented.

Leakage may also occur from Stokes U into V (Lenc *et al.*, 2017), but this is not a concern here because linear polarizations from the corona are negligible at our frequencies and observing bandwidths (*e.g.* Gibson *et al.*, 2016). Of potential concern, however, is possible leakage from V into I . This could add to or subtract from the Stokes I levels, decreasing the reliability of measured polarization fractions. Unlike leakage from Stokes I into the other parameters, the reverse case has not been investigated for the MWA because the polarization fractions of astrophysical sources are generally so low as to make this effect very difficult to characterize and unlikely to significantly impact the results. However, solar radio bursts may have large circular polarization fractions, meaning that Stokes V into I leakage could be a significant contaminant in some cases. We currently have no way to assess or mitigate this contamination, but we anticipate that the effect should occur at a similar or lower level than leakage from Stokes I into V , as the mechanism would be similar but with generally lower magnitudes.

Of concern are sources with high polarization fractions and large leakage fractions. This is relevant mainly for the next section, which focuses on nonthermal active region sources. Assuming that V into I leakage may occur at up to the same level estimated for I into V , this introduces an uncertainty in V/I of less than 1 % for 79 % of the sources and an uncertainty of less than 5 % for 95 % of the sample described by Figure 5. The remainder have uncertainties of 10 % on average, and up to 19 % for one event, due to this effect.

We have chosen to represent this latter population with a different symbol in Figure 5 to indicate that their polarization fractions should be treated with additional skepticism. For Figure 11 in Section 5, we estimate uncertainties on V/I of $\lesssim 3\%$ by combining several effects for two cases where different observations on the same day with different values of L could be compared. These observations correspond to thermal or very weak nonthermal emission for which the polarization fractions are lower than 5%. Potential V into I leakage is therefore not a significant concern in that case and constitutes an average of 14% of the total error bars in Figure 11.

4. Active Region Noise Storm Sources

The most common features in these images are compact polarized sources, the most intense of which are identified here as noise storm continua associated with Type I bursts. This is apparent from the variability in their associated dynamic spectra along with their high polarization fractions. However, as we will see, there are also very weak and weakly-polarized sources for which the source type and emission mechanism is less obvious.

Noise storms are periods of extended burstiness that are associated with active regions and may persist for several days as an active region transits the disk. They are characterized by many distinct, narrowband Type I bursts, often with enhanced continuum emission around the same frequency range (Elgarøy, 1977; Klein, 1998). As our data reflect the background levels during each observation period, our detections correspond to the continuum enhancement, along with any burst periods that could not be filtered out by our baseline procedure because they occurred on timescales less than the 0.5-sec time resolution. Despite decades of study, there are a number of unanswered questions about the nature of Type I bursts. Not all active regions that are productive at other wavelengths produce noise storms, and the non-radio signatures are often scant (Willson, 2005; Iwai *et al.*, 2012; Li *et al.*, 2017), unlike Type II and III bursts, which have obvious associations with CMEs and flares (Cairns *et al.*, 2003; Reid and Ratcliffe, 2014). There is general agreement that both the burst and continuum components of noise storms are produced by plasma emission, largely due to their often high circular polarizations (Aschwanden, 1986; Mugundhan *et al.*, 2018), but what accelerates the electrons is still debated. Small-scale reconnection events (Benz and Wentzel, 1981) or weak shocks associated with upward-propagating waves (Spicer, Benz, and Huba, 1982) are the two leading ideas, and recent work has favored persistent interchange reconnection between open and closed fields at the boundaries of active regions (Del Zanna *et al.*, 2011; Mandrini *et al.*, 2015) or reconnection driven by moving magnetic features (Bentley *et al.*, 2000; Li *et al.*, 2017).

To automatically detect these features in the Stokes V images, we developed a simple algorithm that begins with suppressing any diffuse polarized emission that may be present by applying a Butterworth bandpass filter to the fast Fourier transform (FFT) of each image. The filter aims to flatten the frequency response over a particular passband, in this case the FFT frequencies corresponding to larger spatial scales, without producing sharp discontinuities between the filtered and unfiltered frequencies (Butterworth, 1930). The filtered FFT is transformed back, and the resulting image is thresholded into two binary masks, one for each polarization sense, that include pixels with values above the larger of 10σ or 20% of the maximum value. Ellipses are fit to all of the contiguous regions in the masks, and several criteria are imposed to obtain the final detections. These criteria include ensuring that 1) the signal-to-noise ratio of pixels pulled from the filtered image are above 10σ in the original image and are of the same polarization sense, 2) the areas

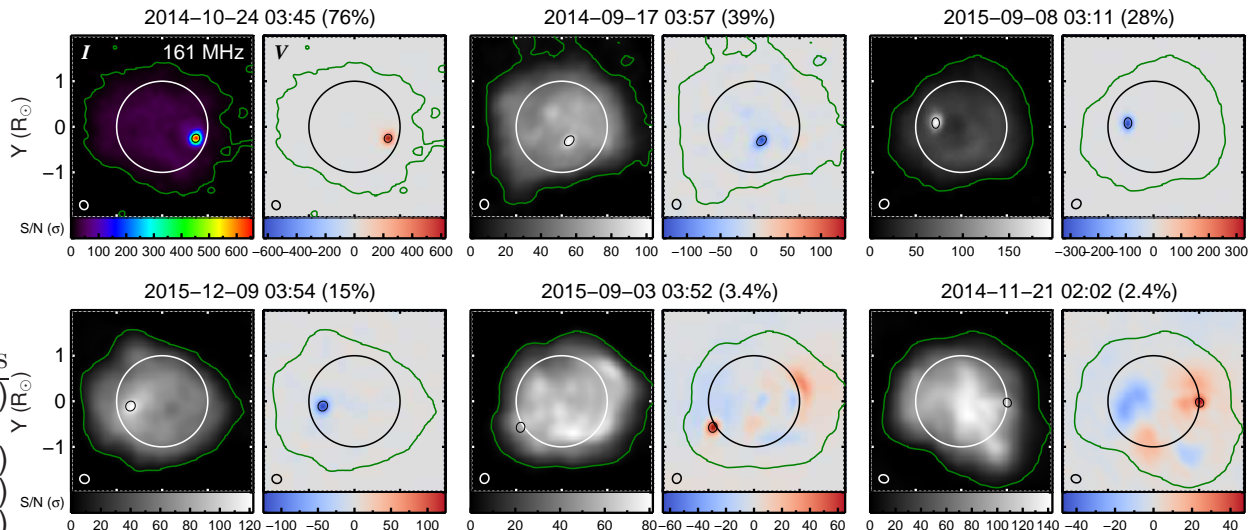


Figure 4. Six randomly chosen examples of compact polarized sources detected at 161 MHz, sorted by polarization fraction. The titles correspond to UTC times followed by the peak polarization fraction in parentheses. The color scales are linear, and the first example is plotted with a different color scheme to better reflect the dynamic range of that observation. Color bar intensities are expressed in units of signal-to-noise [σ], and the green contour reflects the $5\text{-}\sigma$ level in Stokes I . Black ellipses around the sources show the region identified by the source finder algorithm. The large solid circles represent the optical disk, and the ellipses in the lower-left corners represent the synthesized beam sizes.

of the fitted ellipses are within $0.75\text{--}1.5\times$ that of the corresponding synthesized beam for a given frequency, 3) the fitted ellipses have aspect ratios no more than $1.1\times$ that of the synthesized beams, and 4) the masked regions are sufficiently elliptical, which we defined as filling at least 95 % of the fitted ellipse.

These criteria all serve to eliminate false positives that arise from the bandpass filtering, which may amplify noise, introduce artefacts near very bright sources, and/or not entirely suppress the large-scale diffuse emission. Adjusting the tolerance parameters of this algorithm can satisfactorily extract sources from any given image, but finding a set of defaults that could serve the entire dataset was somewhat difficult. We opted to aggressively tune the parameters to eliminate false positives at the cost of excluding false negatives. This procedure is run independently for all of the frequency channels in a given observation. The detections are then grouped across frequencies by checking for overlap among the fitted ellipses. Only sources that are detected in at least three frequency channels are kept and incorporated into the following plots. We find 693 sources with this method from 112 separate regions, and at least one source is found on 64 out of 82 days (78 %). Solar Cycle 24 peaked in April 2014, and our data correspond to between August 2014 and December 2015, meaning that we are examining the early part of the declining phase in the solar cycle. As these features are associated with active regions, we would likely have found a higher fraction of days with at least one noise storm if our observations were shifted one year earlier and a lower fraction if the observations were taken in subsequent years.

Figure 4 shows six randomly-selected examples of these sources at the center of our bandwidth, 161 MHz. They exhibit polarization fractions ranging from 2.4 to 76 % and well represent the range of sources found. Most sources in the full sample are unipolar and are fairly isolated in the polarization images, and those with very low polarization fractions are sometimes embedded in diffuse emission of the same sign. A small number of bipolar sources were also found. This is somewhat inconsistent with White, Thejappa, and Kundu (1992), who found that bipolar sources were nearly as common as unipolar sources in 327

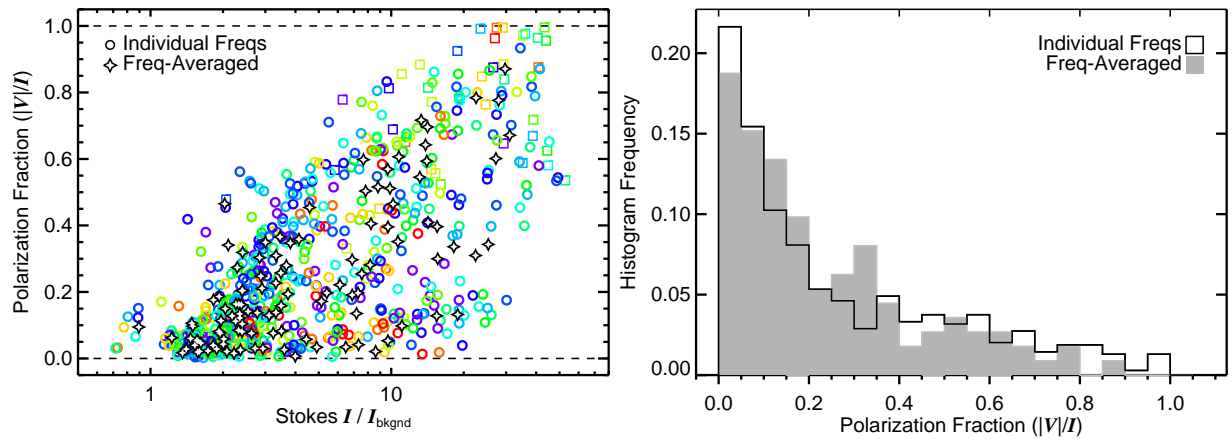


Figure 5. *Left:* Scatterplot of polarization fraction $[|V|/I]$ versus Stokes I intensity for 693 compact polarized sources. Values are measured at the location of peak Stokes V intensity, and the Stokes I intensities are normalized by the median intensity of pixels detected above $5\text{-}\sigma$ $[I_{\text{bkgnd}}]$. Colored circles represent measurements from individual frequency channels; purple refers to the highest frequency (240 MHz) and red refers to the lowest (80 MHz). All sources are detected in at least three channels, representing 112 separate regions, and the stars represent averages across frequency for a given region. Squares indicate the 5 % of sources for which the V/I uncertainty is large (≈ 10 %) due to possible calibration errors that could not be accounted for (see Section 3). *Right:* Histogram of $|V|/I$, where the white region corresponds to the colored circles and the shaded region corresponds to the stars from the left panel.

MHz Very Large Array (VLA) observations. Bipolar sources are presumably less common in our observations because we are looking at lower frequencies for which the emission is generated at a larger height and the spatial resolution is lower. Preliminary analysis has revealed interesting potential anti-correlations in the intensities of the two components of one bipolar source, and this sort of time variability may be explored in future work.

Figure 5 shows a scatterplot of polarization fraction $[|V|/I]$ versus the total intensity divided by the background level $[I/I_{\text{bkgnd}}]$ in the left panel, along with a simple histogram of $|V|/I$ in the right panel. These are plotted both for each frequency channel independently and for averages of the same source detected in multiple channels. The background is defined as the median intensity in pixels detected above 5σ , and the noise level $[\sigma]$ is defined as the standard deviation within a 1-pixel border (1156 pixels) that run along the edge of the 289×289 -pixel ($\pm 3 R_{\odot}$) field-of-view. We find a very broad range of source intensities, ranging from slightly below the background level to 50 times greater, with polarization fractions ranging from a few tenths of a percent to nearly 100 %. The average source has a Stokes I intensity of $7.6\times$ the background level and a polarization fraction of 27 %. The most striking aspect of Figure 5 is the relationship between total intensity over the background and polarization fraction, which are positively correlated with a Pearson correlation coefficient $[r]$ of 0.64.

Figure 6 displays results from one of the few sources in our sample for which we have observations on several consecutive days and for which a compact radio source appears in association with the same active region on each day. The source is polarized between 3 % and 37 % in the same sense in six observations between 9 and 13 November 2015. Our goal here is to investigate a potential relationship between distance from Sun-center and polarization fraction, as previous studies have found noise storms to exhibit higher polarization fractions near disk center. We do not find such a relationship in Figure 6, and instead this exercise further reinforces the positive correlation between total intensity and polarization fraction, which apparently becomes stronger if one considers several observations of the same source. Recall from Section 2 that the observations presented in

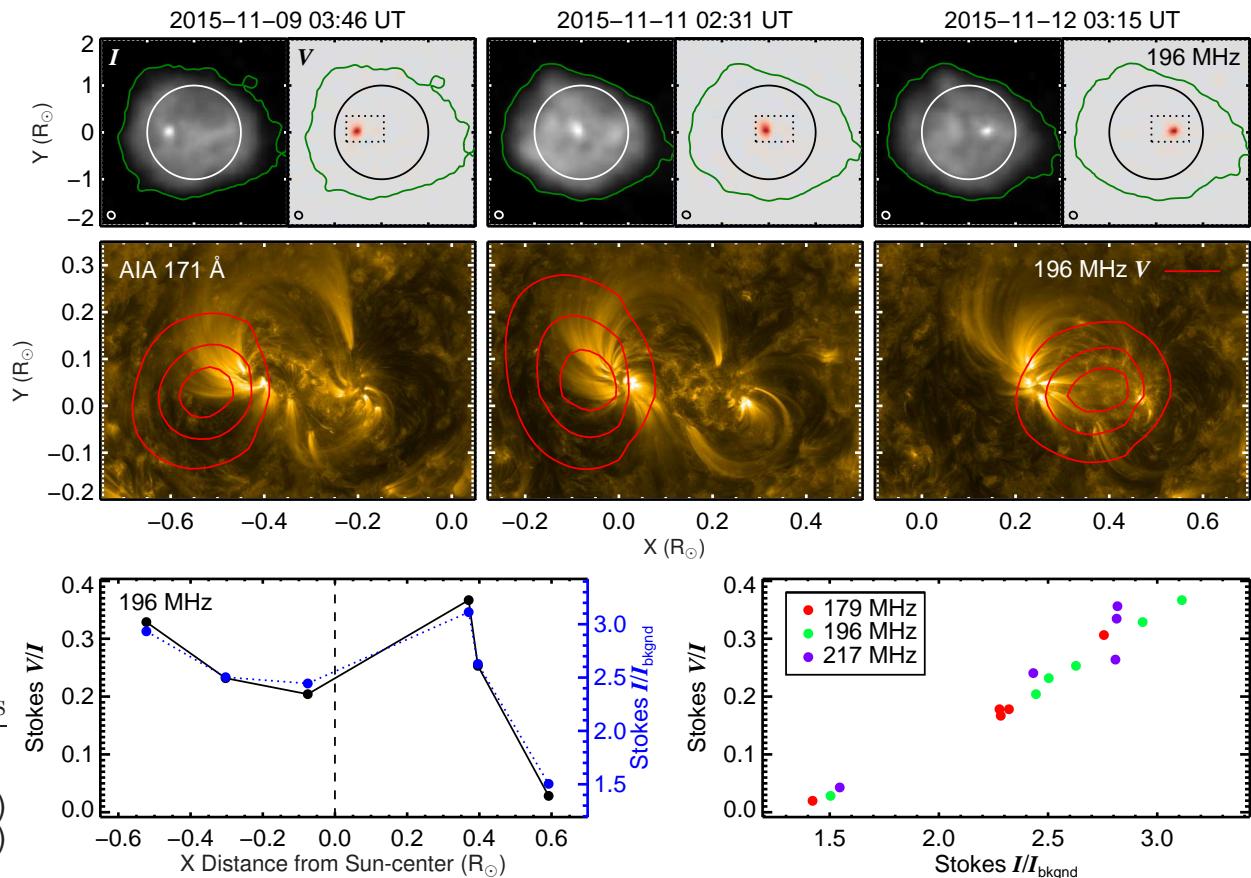


Figure 6. *Top:* The same compact source observed on consecutive days at 196 MHz. *Middle:* Overlays of the 196 MHz circular polarization signal onto 171 Å images from AIA. the field-of-view is marked by the dotted region in the top row, and the contours are at 20, 50, and 80 % of peak intensity. *Bottom:* The left panel plots polarization fraction $[V/I]$ and Stokes I/I_{bkgnd} as a function of horizontal distance from Sun-center at 196 MHz for the same source over five days from 9 to 13 November 2015. The right panel plots the same two parameters against each other for three different frequency channels.

this paper all represent the baseline intensity over 5-min observing periods, constructed from the averages of images with the lowest total intensities. These sources do fluctuate in intensity, so it may be possible to control for the intensity relative to the background and then recheck if the polarization fraction has a longitudinal dependence in a future study, ideally with more observations of individual sources detected on consecutive days.

Figure 6 also overlays circular polarization contours onto 171 Å images from the *Atmospheric Imaging Assembly* (AIA; Lemen *et al.*, 2012) onboard the *Solar Dynamics Observatory* (SDO; Pesnell, Thompson, and Chamberlin, 2012). The radio source is associated with a large active region (AR 12448) and is located over fan-loop structures that represent the bases of loops extending to larger heights. This make sense, as the accelerated electrons that are presumably responsible for this radiation must be able to escape to sufficiently large heights, corresponding to densities that are sufficiently low for low-frequency emission. It is also interesting to note that when the source is east of disk-center, the radio source is associated with the trailing sunspot. Noise storms have long been associated with active regions (*e.g.* Le Squeren, 1963; Gergely and Erickson, 1975; Alissandrakis, Lantos, and Nicolaidis, 1985), and previous observations have found noise storm sources to be more often associated with the leading spot (White, Thejappa, and Kundu, 1992). A natural followup would be to investigate that aspect systematically for the sources detected here. The site of radio emission within the active region also shifts

somewhat in time, with the apparent Carrington longitude jumping by 12 degrees between 11 and 12 November 2015. This is likely due to evolution in the active region shifting the region where the energetic electrons either originate or are able to reach in height.

The main question posed by these results, particularly the scatterplot in Figure 5, is whether or not these sources all represent the same basic phenomenon. Our average polarization fraction (27 %) is lower than previous measurements of noise storm continua. Most studies report similar polarization levels for the Type I burst and continuum components of noise storms, which generally exceed 80 % (Elgarøy, 1977), but sources with lower polarization fractions have also been reported. Dulk, Suzuki, and Sheridan (1984) observed noise storm continua with polarization fractions of $\approx 40\%$, around 15–20 % lower than the associated bursts. As discussed in Section 3, the most intense and likely highly-polarized sources in our dataset could not be included because the leakage mitigation algorithm could not be applied. This diminishes the overall average, but more importantly, our sample includes a large number of weak and weakly-polarized sources that could not have been characterized by previous instruments. For example, the 3 September 2015 source ($V/I = 3.4\%$) shown in Figure 4 is prominent in the polarization map but is visually indistinguishable from the quiet Sun in total intensity. Given that there does not appear to be any separation into distinct populations in Figure 5, we suggest that the data represent a continuum of plasma emission noise storm continua sources with intensities and polarization fractions down to levels that were not previously detectable.

For sources with relatively low total intensities (*e.g.* $I/I_{\text{bknd}} \lesssim 5$; 61 % of the population), where the nonthermal component is not entirely dominant, very low polarization fractions can be explained by there being a mixture of thermal and nonthermal emission within the same resolution element. Recall from Section 1 that the thermal bremsstrahlung and nonthermal plasma emission mechanisms generally produce opposite polarization signs for the same magnetic field orientation, but the plasma emission component is much more highly polarized. Therefore, a pixel may be dominated in total intensity by bremsstrahlung emission while the polarized intensity is dominated by plasma emission. The polarization fraction then rises with intensity relative to the background because the relative contribution from plasma emission increases.

Filling factors and beam dilution are also likely to be important, as the thermal component is likely to fill the resolution element while the nonthermal component may come from a sub-resolution structure. This would mean that the more highly-polarized nonthermal signal is diluted, which would further bring down the polarization fraction. Nonthermal emission sources may not necessarily be intrinsically smaller than the beam size, however. For instance, Mohan *et al.* (2018) found the scattering-deconvolved sizes of type III burst sources to be significantly larger than the PSF. As the total intensity becomes much larger than the background and the nonthermal component becomes entirely dominant, physical effects related to the emission mechanism and radio wave propagation become increasingly important to the interpretation of relatively low polarization fractions in plasma emission sources. As described in Section 1, scattering by density inhomogeneities may reduce the polarization fraction, as can other propagation effects such as mode coupling. These ideas are discussed further in Section 7 in the context of our other results.

5. Coronal Holes

Perhaps the most surprising finding to immediately emerge from these data is a characteristic “bullseye” structure that is frequently exhibited by low-latitude coronal holes

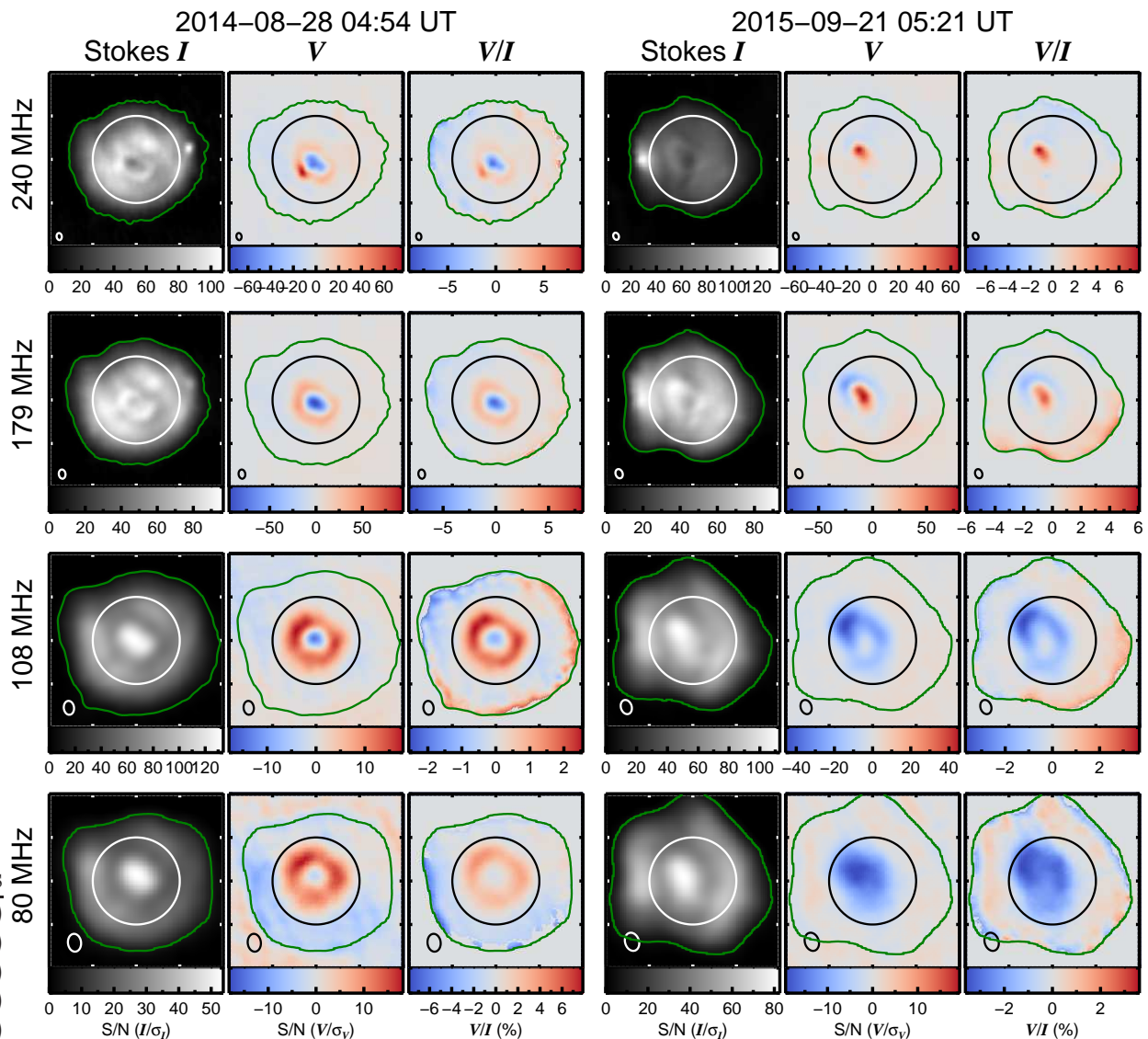


Figure 7. Stokes I , V , and V/I at four frequencies across our bandwidth for two different coronal holes with opposite polarization signatures. Color bar units are in signal-to-noise $[S/N]$ for I and V and percent for polarization fraction $[V/I]$. The green contours represent the 5σ level in Stokes I , the solid circles represent the optical disk, and the ellipses in the lower-left corners represent the synthesized beam sizes.

and, more generally, that coronal holes are the Sun’s most prominent features in circular polarization at low frequencies in the absence of intense noise storm emission. Coronal holes are regions where the magnetic field is open, allowing material to freely flow into interplanetary space to form the fast solar wind (Cranmer, 2009). Because the plasma is not confined by closed fields, the densities inside coronal holes are considerably lower than in the surrounding corona, and they are correspondingly fainter in the soft X-ray and extreme ultraviolet (EUV) observations that are typically used to characterize them. This is also true at our highest frequencies, which can be seen for two different coronal holes in the Stokes I images shown in the upper row of Figure 7.

As frequency decreases across our bandwidth, many coronal holes transition from being relatively dark to relatively bright with respect to their surroundings. This effect had been known from a few previous observations (Dulk and Sheridan, 1974; Lantos *et al.*, 1987; Lantos, 1999; McCauley *et al.*, 2017) and was recently characterized in more detail using MWA observations (Rahman, McCauley, and Cairns, 2019). The mechanism that produces

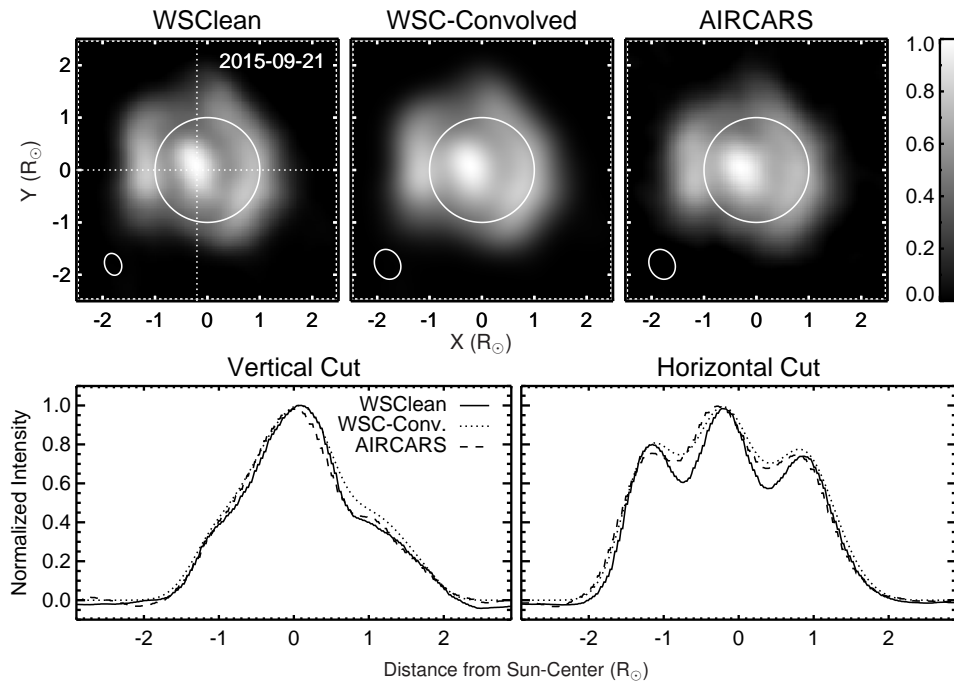


Figure 8. A comparison of the same dataset independently reduced with different calibration techniques and different implementations of the CLEAN algorithm. The Stokes I image at 80 MHz is shown for the 21 September 2015 coronal hole from Figure 7. Our reduction on the left, the AIRCARS reduction on the right, and the AIRCARS image convolved with the WSClean beam is in the middle. Dotted lines in the left panel indicate the cuts shown in lower two panels. The WSClean and convolved AIRCARS images appear nearly identical, and the cuts demonstrate that this is also true quantitatively.

this increase in brightness is unclear, but different authors have suggested that refraction near the coronal hole boundary may systematically redirect emission generated outside of the coronal hole to the interior from an observer’s perspective (Lantos *et al.*, 1987; Alissandrakis, 1994; Rahman, McCauley, and Cairns, 2019). As discussed by Rahman, McCauley, and Cairns (2019), this leads to a ring of enhanced emission around the coronal hole edge, which is apparent in our higher-frequency images but cannot be distinguished at the lower frequencies, likely due to the lower spatial resolution. A corollary of this effect is a ring of diminished intensity in the regions from which the refracted emission originated, which we see prominently in the low-frequency images at the bottom of Figure 7.

The second and third columns of Figure 7 show the corresponding Stokes V and V/I images, respectively. Both coronal holes in Figure 7 exhibit a central polarized component of one sense surrounded by a ring of the opposite sense. The outer ring grows in area as the frequency decreases, while the central component shrinks until it may or may not be completely gone by 80 MHz. This bullseye structure is peculiar in that coronal holes have unipolar line-of-sight (LOS) magnetic field configurations that we expected to result in unipolar Stokes V maps across our entire observing band. We therefore first consider if the feature might be an instrumental or calibration artefact. While we cannot validate this signature with a completely independent observation and data reduction procedure, we have strong evidence to believe that this structure is real for the reasons outlined below.

First, we can validate the structure seen in Stokes I with an independent reduction. Figure 8 compares our 80 MHz image of the 21 September 2015 coronal hole, which was produced using WSClean, to an image produced using the AIRCARS pipeline (Mondal *et al.*, 2019). AIRCARS uses an entirely different calibration scheme through iterative self-

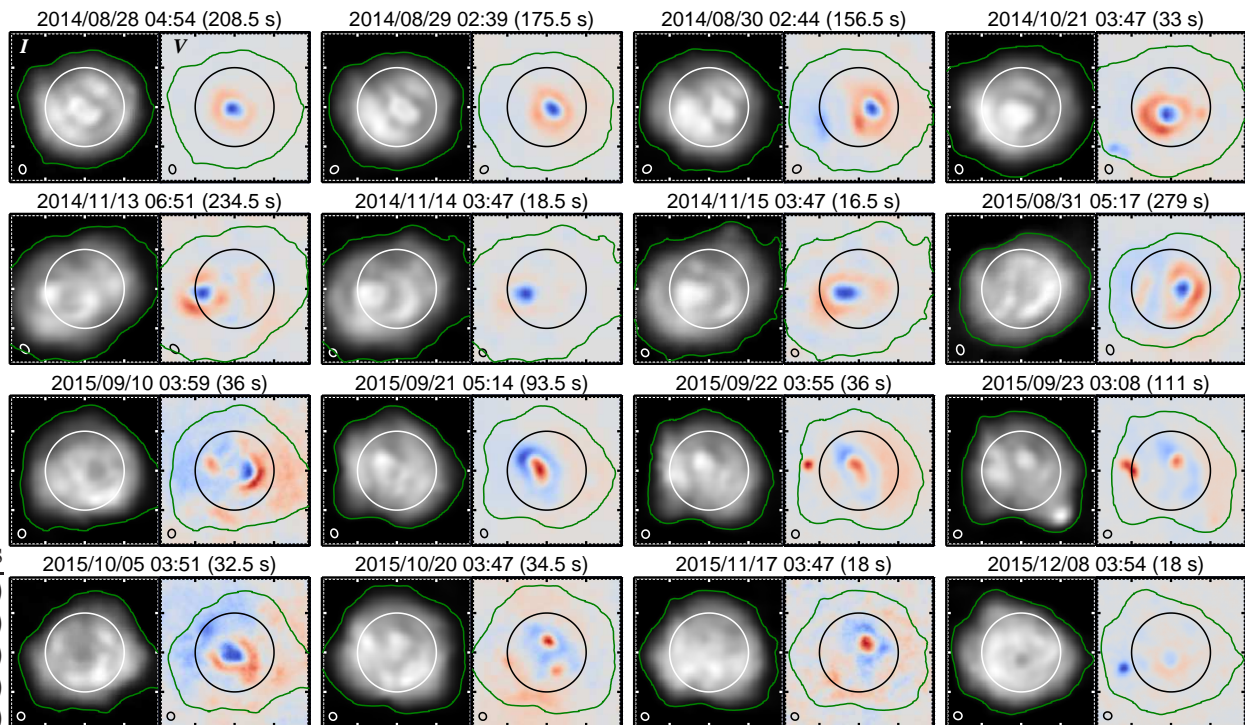


Figure 9. Mosaic of coronal hole observations at 161 MHz, with Stokes I on the left and Stokes V on the right. The green contours show the $5\text{-}\sigma$ levels for Stokes I , the solid circles denote the optical limb, and ellipses in the lower-left corners reflect the synthesized beam sizes. The titles correspond to UTC times followed by the effective integration times in parentheses. Linear color scales are as in Figure 7, with red, blue, and gray corresponding to positive, negative, and zero Stokes V intensity, respectively. Images for all 12 frequency channels can be seen in an animated version of this figure available in the [online material](#). Note that some dates do not have observations at all frequency channels because of calibration failures, and two observation periods exhibit bright nonthermal sources at higher frequencies that prevent the coronal hole structure from being visible due to limited dynamic range.

calibration on the Sun itself without the need to observe a separate calibrator source. This approach is advantageous in that the calibration is tuned to the specific observation of interest, which may greatly improve the dynamic range, but it cannot yet be used for polarimetry. Our method determines the calibration solutions solely from a known calibrator source, generally observed before or after an observing campaign of several hours. Figure 8 shows that we obtain nearly identical results from the two pipelines. Both methods do use the CLEAN algorithm for deconvolution, as is the standard, although implemented through different software packages. However, we can be confident that we are not seeing an artefact of the CLEAN because the features of interest are also present in the undeconvolved “dirty images”.

We are also confident that the Stokes I into V leakage subtraction method has not introduced this feature. As described in Section 3, the leakage fraction (L) is assumed to be constant across the relatively small spatial scale of the Sun based on results from widefield astronomical studies (Lenc *et al.*, 2017). Because L is constant, varying it changes the fractional polarization level without changing the qualitative structure. Figure 1 illustrates how the subtraction algorithm works for one of the same coronal hole observations shown in Figure 7, and the animated version of Figure 1 ([available online](#)) shows how the “corrected” images look as a function of L . The animation shows that the polarization reversal bullseye pattern remains for all values of L until reaching the extremes, where 80–100 % of pixels across the Sun are too highly polarized of the same sense to be believable. Further, varying

L by just 1–2 % on either side of the value obtained from the correction algorithm quickly pushes into this extreme case. And even at the extremes, the qualitative ring pattern remains as a sharp change in polarization fraction instead of a reversal.

Next, this polarization ring structure is not rare and seems to be characteristic of low-latitude coronal holes across our dataset. We have 28 separate observations of 13 different coronal holes in 2014 and 2015 that exhibit this effect. A mosaic of examples is shown in Figure 9 at 161 MHz, the center of our observing band, and the other channels can be seen in the corresponding animation. Several coronal holes in the mosaic are shown on consecutive days, and they move with the solar rotation as expected. This structure is not observed in association with other solar features, despite noise storms often having similar appearances in total intensity at the lowest frequencies. Therefore, from both a data reduction perspective and with respect to its association with solar features, the bullseye feature does not appear to be consistent with an instrumental effect. Moreover, while this feature is a surprise to us, we do find various points of consistency between the observations and our expectations that will be discussed later.

Figure 10 overlays contours of the 161 MHz polarimetric signal from the two coronal holes shown in Figure 7 onto 193 Å images from the AIA and LOS magnetograms from the *Helioseismic and Magnetic Imager* (HMI; Scherrer *et al.*, 2012) onboard the SDO. These two coronal holes were chosen for this exercise because they have opposite polarization signatures, which is consistent with them having opposite magnetic field configurations at the photosphere, and because we have two observations of each on the same day, which we will use to estimate the uncertainty in V/I . The last column of Figure 10 overlays the polarization contours onto the LOS component [B_{LOS}] of a potential field source surface (PFSS; Schrijver and De Rosa, 2003) model at a height roughly corresponding to that of the radio limb. The models were obtained from the PFSS module in SolarSoft IDL and manipulated using the FORWARD codes. A height of 1.27 R_{\odot} is used, which corresponds to the height of the plasma frequency layer at 161 MHz in a $3\times$ Newkirk (1961) density model.

Crucially, the central polarized components do not match the orientation of B_{LOS} , as would be expected from the thermal bremsstrahlung process that is assumed to be the dominant, if not sole, emission mechanism in coronal holes. This effect is further characterized in Figure 11, which plots cuts through the same two coronal holes in Stokes I , V , and V/I . The I and V cuts are normalized by the background intensity in Stokes I , which we define as the median pixel intensity for pixels detected above $5\text{-}\sigma$. The gradual transition with decreasing frequency of both coronal holes from being dark to bright relative to the background is nicely illustrated by the Stokes I curves for both examples, as is the oppositely-oriented ring structure in Stokes V . Note that the large spikes in V/I near the ends of the slits are in locations where both the total intensity and polarized signals approach the noise level, making the fractional polarizations unreliable.

While the overall pattern is similar for both coronal holes, the behavior of the central component is somewhat different in each case. The rightmost panels (g and h) of Figure 11 show the peak V/I for the central and ring components. The central component is most highly polarized ($\approx 5\text{--}8\%$) at our highest frequency (240 MHz) and gradually decreases in polarization fraction with decreasing frequency. For the 28 August 2014 example, the central component falls to nearly 0 % polarization at 80 MHz but remains of the same sign at all frequencies, whereas the 21 September 2015 examples crosses 0 % around 108 MHz and gradually approaches the same polarization level as the ring component. The latter scenario is somewhat more common in our experience. That is, by 80 MHz, the entire

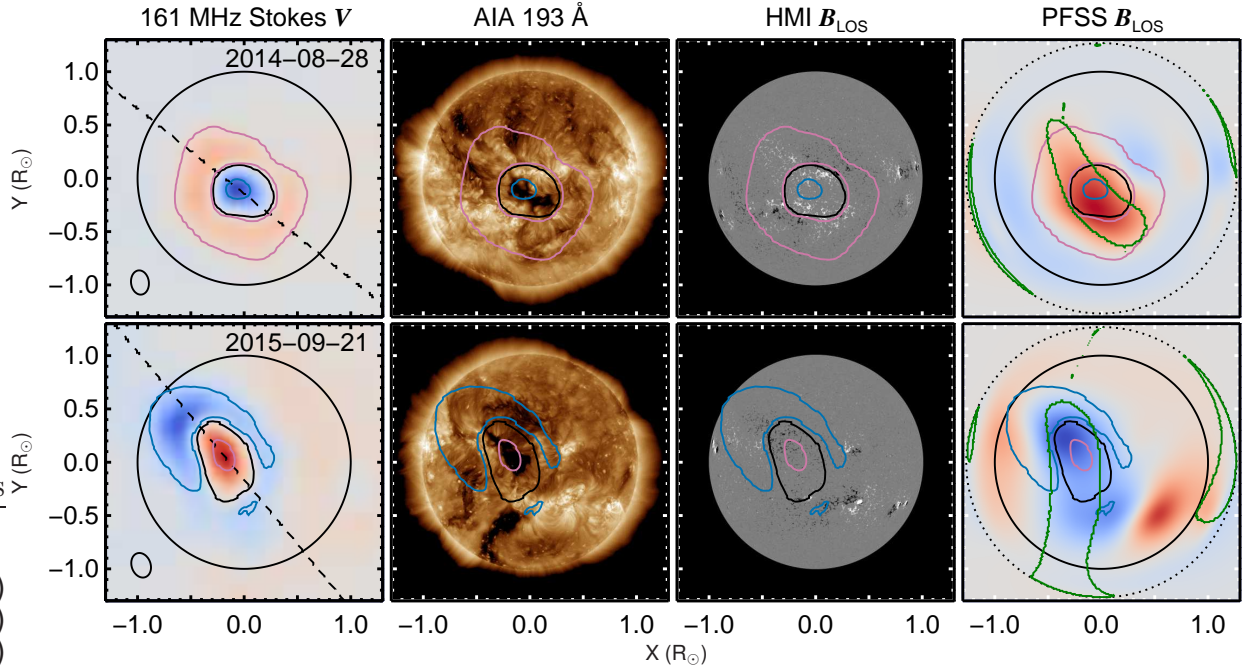


Figure 10. The first column shows Stokes V at 161 MHz for the two coronal holes from Figure 7. The solid black circle represents the optical disk, the black contour is where $V = 0$ in that region, the blue contour is at 75 % of the central components' maxima, and the pink contour is at 25 % of the ring components' maxima. The dashed lines denote the slits used in Figure 11. The second and third columns plot AIA 193 Å and HMI line-of-sight [B_{LOS}] magnetograms with the V contours from the first column. The last column shows the B_{LOS} component of the PFSS model at a height roughly corresponding to that of the radio limb ($1.27 R_{\odot}$). Red, blue, and gray colors represent positive, negative, and zero B_{LOS} , respectively, and green contours represent open field regions in the model at that height.

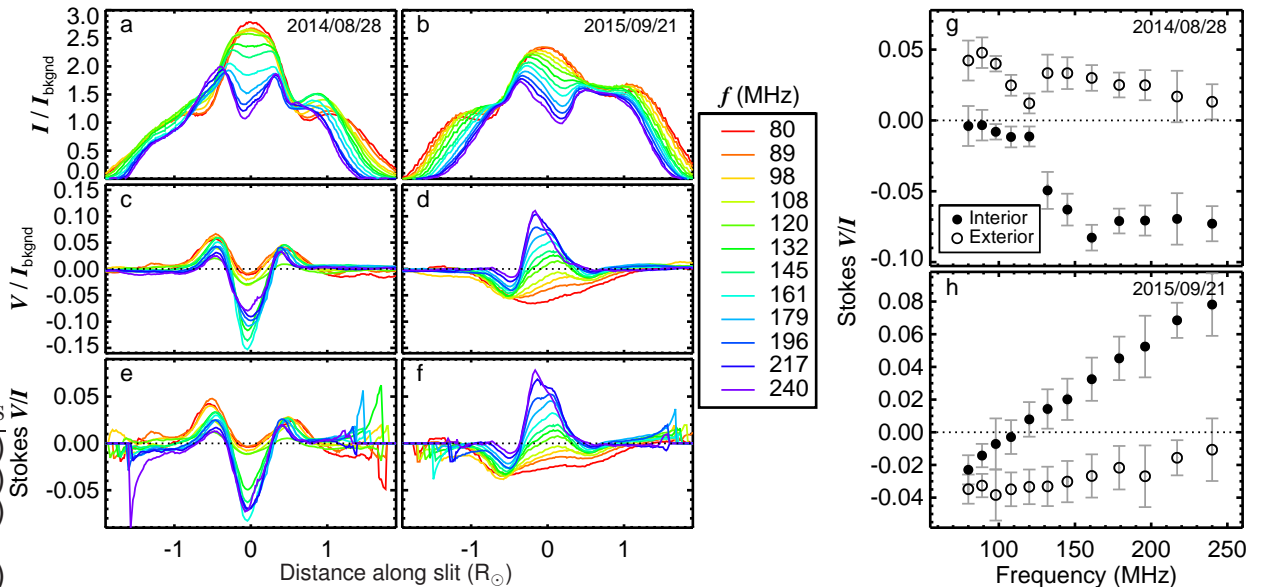


Figure 11. (a–b): Stokes I intensity for each frequency channel along the slits shown in Figure 10 through two coronal holes on 28 August 2014 (left) and 21 September 2015 (right). (c–d): Stokes V intensities along the same slits. Panels a–d are shown in normalized units, where the normalization factor corresponds to the median Stokes I intensity of pixels detected above 5σ (*i.e.* the background level). (e–f): The corresponding Stokes V/I fractional polarization levels. (g–h): Peak Stokes V/I for the coronal holes' interior (filled circles) and exterior ring (open circles) components as a function of frequency.

source is typically polarized in the same sense expected by bremsstrahlung emission and at a similar level, often with a small dip in polarization fraction at the center where the source is oppositely-polarized at higher frequencies.

The uncertainties in panels g and h of Figure 11 are the combination of measurement noise and three effects related to the leakage subtraction algorithm described in Section 3. The first is the range of values found by varying the minimization parameter $r_{c,\text{thresh}}$ in Equation 3 between 0.3 and 0.8 %, along with varying the pixels included in the operation between those detected above 5σ and those detected above 15σ . The second is the difference in polarization fraction at the same locations in two observations separated by 2–3 hours, and the third is the potential for unaccounted for leakage of Stokes V into I at up to the same level as that measured for I into V . These combined uncertainties in V/I average $\pm 1.2 \%$ and are as large as $\pm 2.9 \%$. In both cases, the sign of the leakage fraction flips for each frequency channel between the two observations as the Sun moves to different locations in the primary beam with respect to the phase center. (The MWA does not continuously track an object and instead has a set of discrete pointings that may be changed after every ≈ 5 -min observing period.)

Despite the sign change in the leakage artefact between observations separated by 2–3 hours, after implementing the subtraction algorithm, the polarization fraction remains consistent to within 1 % for a given location and frequency channel. However, a sharp discontinuity remains between the 120 and 132 MHz channels in the 28 August 2014 observation. The leakage is more severe in this observation as compared to the 21 September 2015 data, and the sign of the leakage also changes between those two channels. The discontinuity in the polarization fraction trend shown in Figure 11g is therefore likely to be a calibration artefact that cannot be removed by uniformly implementing our correction algorithm. This suggests an additional source of uncertainty in the polarization fraction that is not accounted for by the methods described in the previous paragraph. However, note that leakage affects the polarization level uniformly across the image and cannot warp the qualitative structure observed because the leakage does not vary on the small angular scale of the Sun, given what we know from widefield astrophysical observations.

The puzzle with respect to this feature is again the fact that the polarization of the central component does not match the sign expected from thermal bremsstrahlung emission. We will discuss possible interpretations for this in Section 7.

6. The Large-Scale Quiescent Structure

As mentioned in Section 1, the thermal bremsstrahlung process that dominates quiescent coronal emission at low frequencies produces a slight circular polarization signature in a magnetized plasma that depends primarily on the line-of-sight magnetic field strength. Absent of other emission mechanisms, a positive LOS field should produce a positive Stokes V signature of up to a few percent that depends on the field strength.

Figure 12 shows Stokes I , V , and V/I images on four different days for which the polarimetric signature is not dominated by a bright noise storm source or disk-center coronal hole. These days were also selected to have a mixture of positive and negative Stokes V regions so that we can compare the structure to that of the LOS field. The fourth column of Figure 12 shows the LOS magnetic field direction and strength in the corresponding PFSS model. The dotted circle indicates the height at which the model LOS field is shown, which is chosen to be roughly that of the radio limb, and the plane-of-sky field is shown beyond the dotted circle. This height is $1.49 R_{\odot}$ at 89 MHz and corresponds to the height

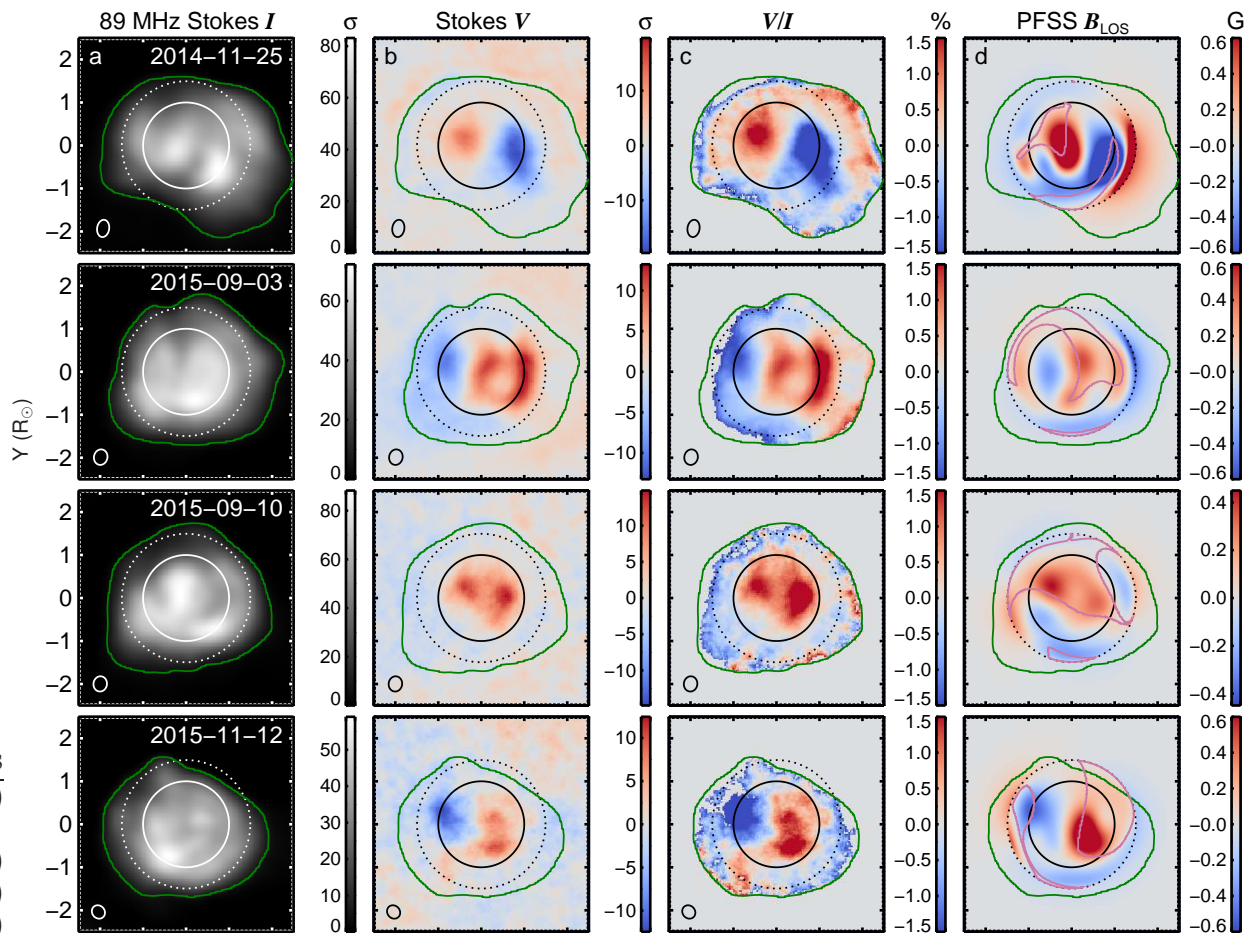


Figure 12. Columns a–c show Stokes I , V , and V/I images at 89 MHz on four different days for which a single compact region does not dominate the total intensity. The solid circles denote the optical limb, and the green contours show the 5σ level for Stokes I . Ellipses in the lower-left corners reflect the synthesized beams. Column d shows the line-of-sight magnetic field strength [B_{LOS}] in the PFSS model at a height of $1.49 R_{\odot}$, which roughly corresponds to the height of the radio limb at 89 MHz and is indicated by the dotted circles in each panel. The pink contours indicate open field regions in the model. Color bar units are in signal-to-noise [σ] for Stokes I and V , percent for V/I , and Gauss [G] for the field model. An animated version of this figure that shows all 12 frequency channels is available in the [online material](#).

of the plasma frequency layer in a 3-fold Newkirk (1961) density model. Pink contours indicate the open-field regions in the model at the same height, which were determined using the “topology” keyword in the FORWARD code. It is immediately apparent that the Stokes I and V maps show very different morphologies in general. Regions with the highest polarized intensities are often not straightforwardly correlated with those of highest total intensity. It is also interesting to note that larger polarized intensities are often associated with open field regions, which is also consistent with the coronal hole observations from the previous section. While we have not investigated this effect systematically, it may be due to there being lower densities and lower density contrasts between adjacent regions in open field regions, which then reduces the depolarizing effect of scattering by density inhomogeneities.

Figure 12 demonstrates that the Stokes V structure at our lowest frequencies is generally well-matched to the LOS field, at least near disk center, and that the sign of Stokes V is broadly consistent with that expected from thermal bremsstrahlung emission given the LOS field orientation. The boundaries between opposite polarization signs are roughly aligned with polarity inversion lines in the model. The agreement tends to diminish with

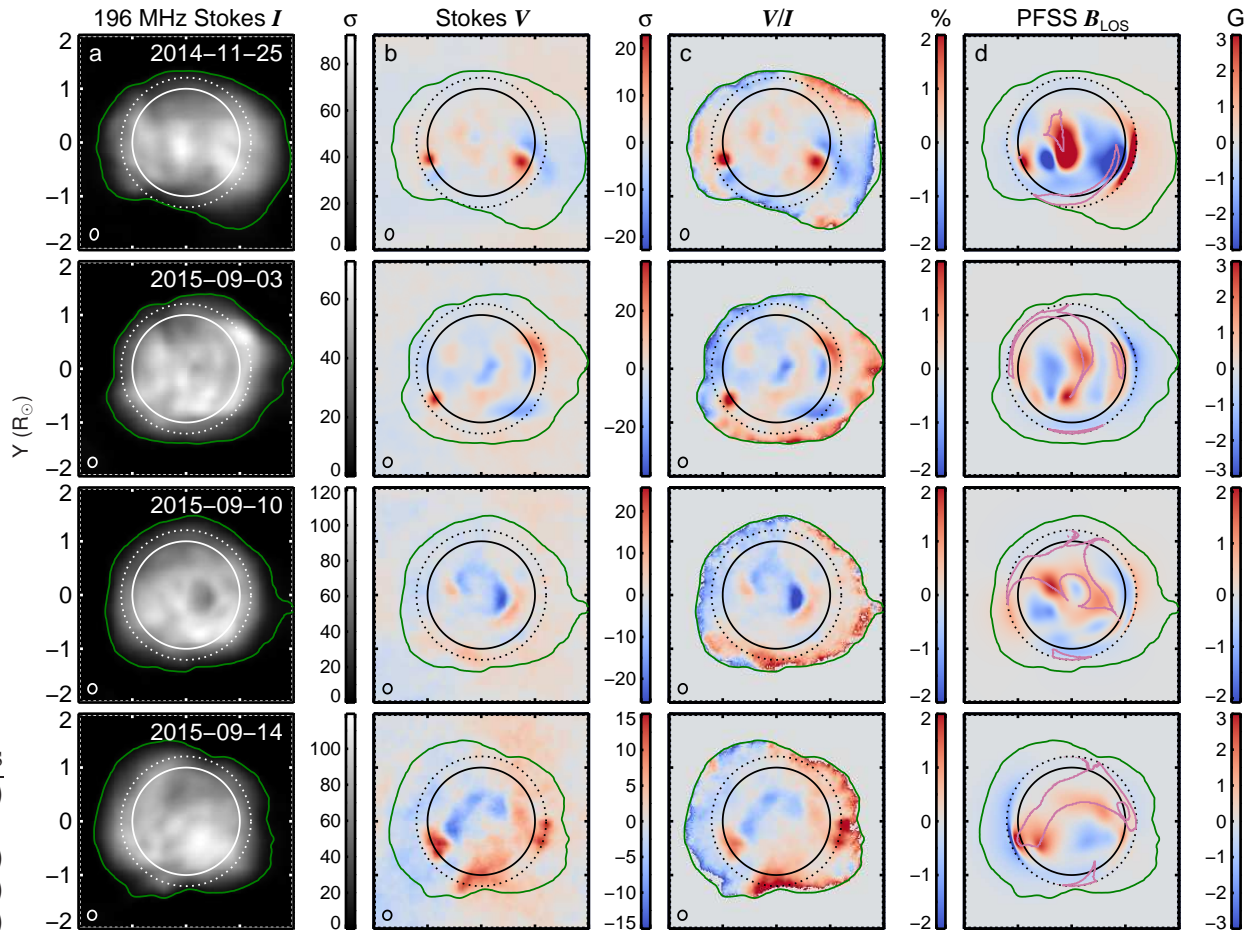


Figure 13. Columns **a** – **c** show Stokes I , V , and V/I images at 196 MHz on four different days for which a single compact region does not dominate the total intensity. The days are the same as Figure 12 except for the last row. The solid circles denote the optical limb, and the green contours show the 5σ level for Stokes I . Ellipses in the lower-left corners reflect the synthesized beams. Column **d** shows the line-of-sight magnetic field strength [B_{LOS}] in the PFSS model at a height of $1.21 R_{\odot}$, which roughly corresponds to the height of the radio limb at 196 MHz and is indicated by the dotted circles in each panel. The pink contours indicate open field regions in the model. Color bar units are in signal-to-noise [σ] for Stokes I and V , percent for V/I , and Gauss [G] for the field model.

distance from disk center, which is likely due to two effects. First, low-frequency radio emission is heavily influenced by propagation effects, namely refraction, scattering, and mode coupling, that can influence the polarization sign and fraction, and these effects become more pronounced near the limb (Shibasaki, Alissandrakis, and Pohjolainen, 2011). Second, although the polarization fraction is expected to be highest off the limb (Sastry, 2009), the intensity is much lower there. The third column of Figure 12 shows that we often do find relatively high polarization fractions toward the radio limb, but these pixels are very close to the noise level in Stokes V and we do not regard them as reliable. Missing pixels in the Stokes V/I images inside the green 5σ Stokes I contour are censored because they have polarization fractions greater than 1.5 % but Stokes V signals below 5σ .

Figure 13 shows the same parameters as Figure 12 but at 196 MHz. The same observation periods are used in the first three rows, but the fourth row is different because the 12 November 2015 observation becomes dominated by a noise storm source at higher frequencies. First, we note that the polarized quiet Sun emission is more localized at 196 MHz compared to 89 MHz, which is likely the combination of at least three effects. First, the spatial resolution is simply lower at lower frequencies. Second, lower frequency

emission is produced at larger heights where the corona is somewhat less finely structured, with smaller contrasts in magnetic field and density between adjacent regions. Third, lower-frequency emission is more strongly scattered, which leads to increased angular broadening with decreasing frequency.

Figure 13 also exhibits much less straightforward agreement between the LOS field orientation and the polarization structure. This is a gradual transition with increasing frequency that we cannot attribute to instrumental effects because we never observe such an inversion for the noise storm sources that are detected across our entire observing band from 80 to 240 MHz. Some of the differences between the Stokes V sign and that expected from the LOS field orientation can likely be attributed to the same unknown effect present in the coronal hole observations from Section 5. For instance in the 10 September 2015 and 14 September 2015 observations, there are coronal holes near the west limb and north pole, respectively, that exhibit this effect. However, those regions aside, there is still not the same alignment between opposite polarization signs and LOS field polarity inversion lines that we see at low frequencies.

One possible explanation for the discrepancies at higher frequencies is simply the accuracy and resolution of the potential field model. Higher frequencies correspond to lower heights, and the true coronal magnetic field becomes increasingly non-potential closer to the surface, with larger contrasts between adjacent regions. This is also true for the density and temperature, which also affect the polarization signal to some extent and will be important for future forward modeling efforts. However, our impression is that physical effects are also likely to be important, and we discuss some possibilities in the next section.

7. Discussion

These data offer an opportunity to probe the coronal magnetic field at heights and scales that are not easily accessed with other instruments. The intent of this article is to introduce the data and survey the range of features observed in this new regime. In a forthcoming study, we will directly compare the magnetic field strength and structure implied by our observations to model predictions of the thermal bremsstrahlung emission implied by different global models. Preliminary results suggest that we can successfully generate synthetic Stokes V/I images that reproduce the low-frequency polarization structure near disk center, but we have yet to explicitly compare the field strengths implied by the observed polarization fractions.

While these preliminary results are encouraging, there are a number of questions that will require deeper investigation. The most perplexing of these is perhaps the bullseye structure in Stokes V described in Section 5, which is found for many low-latitude coronal holes. At our higher frequencies (≤ 240 MHz), low-latitude coronal holes often exhibit a central circularly-polarized component surrounded by a full or partial ring of the opposite sense, and the central component is of the opposite sign than would be expected from thermal bremsstrahlung, the presumed emission mechanism. With decreasing frequency, the central component diminishes and the ring expands. By 80 MHz, there may be some trace of the central component remaining or the region may be entirely of the sign expected by bremsstrahlung emission.

We have two suggestions for what may be responsible for this effect. The first has to do with differential refraction of the x - and o -modes. The two modes have slightly different group velocities within the plasma and therefore slightly different refractive indices, as is often observed in ionospheric propagation experiments at Earth (Melrose, 1986). It may be

possible to separate the two modes sufficiently via refraction so as to produce a polarization sign that is the opposite of that expected by bremsstrahlung emission. For example, the refractive index of the x -mode is further below unity than the o -mode. Emission generated by denser plasma at the edge of a coronal hole may refract at the coronal hole boundary, with the x -mode refracting more strongly in the radial direction, producing an enhancement of x -mode around the perimeter and o -mode near the center. Propagation effects do seem to be particularly important in coronal holes, as they are the preferred explanation for why some coronal holes are significantly brighter than their surroundings at low frequencies (Alissandrakis, 1994; Rahman, McCauley, and Cairns, 2019). However, this later question has not been resolved, and it is not obvious to us how this polarization signal would be produced. Ray tracing simulations, such as those done by Benkevitch *et al.* (2012) or Vocks *et al.* (2018), are likely needed to investigate this further.

A second possibility that we regard as less likely is that the central polarized component is produced by weak plasma emission, which generally produces the opposite sign in circular polarization compared bremsstrahlung for the same line-of-sight field. Because plasma emission may be up to 100 % circularly polarized, it is possible for the total intensity to be dominated by thermal bremsstrahlung emission while the polarized component is dominated by plasma emission. This is what we expect to be happening in the low-intensity and weakly-polarized active region sources described in Section 4. For coronal holes, the driver of this plasma emission might be the transition region network jets discovered by the Interface Region Imaging Spectrograph (Tian *et al.*, 2014). These jets are continuously generated throughout the transition region, but they are particularly common and intense inside coronal holes (Narang *et al.*, 2016). They strongly resemble the coronal X-ray jets associated with Type III bursts, and some attribute the network jets to small-scale reconnection events (Tian *et al.*, 2014; Kayshap *et al.*, 2018). However, the network jets also resemble chromospheric Type II spicules and may instead be driven by shocks (Cranmer and Woolsey, 2015) or heating fronts (De Pontieu, Martínez-Sykora, and Chintzoglou, 2017). If these jets are associated with reconnection or shocks, then nonthermal electrons capable of producing plasma emission may be expected at least to some extent by analogy with solar radio bursts. We may see this emission only in coronal holes because the densities there are low enough that the plasma levels associated with our highest frequencies are in, or very close to, the transition region. This idea could be explored observationally through examining variability in the polarization signal and comparing that to the typical jet timescales.

A mixture of plasma emission and thermal emission may also help to explain why our higher-frequency Stokes V maps are not well-correlated with the LOS field structure. One of the MWA's main contributions thus far has been to demonstrate the prevalence of very weak nonthermal emissions (Suresh *et al.*, 2017). Sharma, Oberoi, and Arjunwadkar (2018) report that up to 45 % of the total intensity outside of nominal burst periods may be nonthermal during moderately active periods, and preliminary imaging analyses suggest that nonthermal components are present to varying degrees in every environment. These nonthermal emissions are attributed to plasma emission, which again is generally much more highly polarized and of the opposite sign compared to bremsstrahlung. A relatively minor total intensity contribution from plasma emission would therefore have a much greater impact on the circularly-polarized intensity and may be capable of reversing the observed sense from that expected from thermal emission. The polarization fraction could also potentially be used to disentangle the contributions of both mechanisms.

Mode coupling effects associated with quasi-transverse (QT) regions are also likely to be important at least in some regions and may contribute to differences between the observed polarization sense and that straightforwardly expected from a particular emission mechanism, along with reductions in the polarization fraction expected from plasma emission sources. QT regions refer to when the magnetic field orientation is nearly perpendicular to that of the emission region, such that there is no magnetic field component along the ray path. Passing through such a region may cause the circular polarization sign to reverse if the emission frequency is below a certain threshold that depends on the plasma properties (Cohen, 1960; Zheleznyakov and Zlotnik, 1964; Melrose and Robinson, 1994). This concept is very important to the interpretation of polarization reversals and associated magnetic field diagnostics in high-frequency microwave observations (*e.g.* Ryabov *et al.*, 1999; Altyntsev *et al.*, 2017; Shain, Melnikov, and Morgachev, 2017; Sharykin, Kuznetsov, and Myshyakov, 2018). At lower frequencies, QT regions are also invoked to explain the polarization properties of noise storms (Suzuki and Sheridan, 1980; White, Thejappa, and Kundu, 1992), Types U and N bursts (Suzuki and Sheridan, 1980; Kong *et al.*, 2016), and zebra patterns in Type IV bursts (Kaneda *et al.*, 2015). A natural place to start investigating the importance of QT regions in our observations would be by comparing the polarization sense of the active region noise storm sources from Section 4 to that expected from the magnetic field orientation assuming o -mode polarization from plasma emission.

Lastly, it would be useful to explore improving our calibration approach by imposing constraints specific to solar observing. We have introduced a strategy, adapted from the astrophysical literature, to mitigate an artefact referred to as “leakage,” whereby the polarimetric signal is contaminated by some fraction of the total intensity signal. This is described in Section 3. While we have demonstrated that our approach is reasonably effective, it is clearly not perfect given the discrepancies occasionally observed between adjacent frequency channels, as illustrated by Figure 11g. A better solution may be available by imposing constraints based on the expectation that we can generally assume that the linear polarizations (Stokes Q and U) are zero because Faraday rotation destroys the linear polarization signal over most observing bandwidths. Assuming Q and U are zero implies that the XX and YY instrumental polarizations are equal, and this constraint may be applied for each antenna in visibility space, allowing for a direction-dependent polarization calibration. We do not yet know the feasibility of this approach, and new software tools would need to be developed to implement it.

8. Conclusion

We have presented the first spectropolarimetric imaging of the Sun using the MWA. These are the first imaging observations of the low-frequency corona that are capable of measuring the weak polarization signals outside of intense burst periods. We reviewed the two dominant emission mechanisms, thermal bremsstrahlung and plasma emission, and how their expected polarization signatures relate to our observations. Our data were taken from over 100 observing runs near solar maximum, and we surveyed the range of features detected in quiescent periods. These observations can be used to diagnose the coronal magnetic field at heights and scales for which the available data constraints are limited, and this will be the focus of future work. Our contributions are as follows:

- We introduced an algorithm to mitigate an instrumental artefact known as “leakage,” whereby some fraction of the total intensity [Stokes I] signal contaminates the circular

polarization [Stokes V] images (Section 3). Leakage occurs due to differences between the actual instrumental response and the primary beam model used to convert images of the instrumental polarizations into Stokes images. These errors may be due to imperfections in the beam model itself or to other effects that change the instrument’s effective response, such as individual antenna failures or, importantly, the practice of applying calibration solutions from a calibrator source at one pointing to the target source at another pointing. We adapted an approach used for astrophysical MWA studies, which show that the leakage varies negligibly over the spatial scale of the Sun. Given that most of the pixels in our images should be very weakly polarized based on our expectations for thermal bremsstrahlung emission, we determined the leakage fractions with an algorithm that minimizes the number of pixels with polarization fractions $[|V/I|]$ greater than 0.5 %.

- We developed and employed a source finding algorithm that detected around 700 compact sources in the Stokes V images (Section 4). Only sources detected in a least three frequency channels were analyzed further, corresponding to 112 distinct sources found at multiple frequencies. The intensities of these sites ranged from slightly below the background level to $60\times$ greater than the background. Their polarization fractions ranged from less than 0.5 % to nearly 100 %. At least one of these sources was present on 78 % of our observing days, and we found a positive correlation between the total intensity over the background and the polarization fraction ($r = 0.64$). The high-intensity sources with large polarization fractions are noise storm continua sources produced by plasma emission and associated with active regions. As there is no obvious separation of these sources into distinct populations, we suggest that they represent a continuum of plasma emission sources down to intensities and polarization fractions that were not previously observable in imaging observations. Although the plasma emission theory predicts 100 % circular polarization for fundamental emission, very low polarizations can be explained in this context through three effects. First, the weaker sources may still be dominated by thermal bremsstrahlung emission with a minor contribution from plasma emission that then dominates the polarized component. Second, the plasma emission sites may often be considerably smaller than the beam size, leading to beam dilution that smears the polarized signal across a larger area. Third, scattering by density irregularities may also reduce the polarization fraction, even for very intense sources.
- We reported the discovery of a “bullseye” polarization structure often associated with low-latitude coronal holes in which one polarization sense is surrounded by a full or partial ring of the opposite sense (Section 5). The polarization of the central component is of the opposite sign from that expected from thermal bremsstrahlung, the presumed emission mechanism. Moving from our highest frequency (240 MHz) to our lowest (80 MHz), the central component diminishes and the ring expands. Some coronal holes continue to exhibit the ring structure at 80 MHz, while others are unipolar in Stokes V with a sense that matches that expected for bremsstrahlung emission. This effect was observed in 28 separate observations of 13 different coronal holes. We validated the Stokes I structure with an independent data reduction, and we noted that similar total intensity structures associated with noise storms never exhibit this effect. We speculated that the structure may be the result of propagation effects, namely refraction, that separate the x - and o -modes, but ray tracing simulations are needed to test this. Alternatively, we suggested that the polarization signature may be produced by weak plasma emission produced by the recently-discovered transition region network jets that are particularly prevalent inside coronal

holes.

- We showed that at our lowest frequencies, the large-scale Stokes V structure is reasonably well-correlated with the line-of-sight magnetic field structure obtained from a global potential field source surface model (Section 6). The boundaries between opposite polarization signs are generally aligned with polarity inversion lines in the model, with the polarization sign matching the expectation from thermal bremsstrahlung emission given the LOS field orientation. The correspondence is best near disk center and diminishes toward the limb, where propagation effects become increasingly important and the signal-to-noise decreases. At our highest frequencies, there is little straightforward agreement between the LOS field orientation and the polarization sign. This may be due to the limited accuracy of the potential model, as the coronal field becomes increasingly non-potential at lower heights where higher-frequency emission generated. However, we suspect that physical effects are also important. These may include a mixture of thermal and non-thermal emission in the same region, along with propagation effects such as refraction and polarization reversals due to quasi-transverse (QT) regions.

Acknowledgments This work was primarily supported by the Australian Government through an Endeavour Postgraduate Scholarship. P. McCauley acknowledges the Asian Office of Aerospace Research and Development (AOARD) of the United States Air Force Office of Scientific Research (AFOSR) for travel support through the Windows on Science (WOS) program. I. Cairns and J. Morgan acknowledge support from AFOSR grants FA9550-18-1-0671 and FA9550-18-1-0473, respectively. We thank Don Melrose and Sarah Gibson for helpful discussions. We also thank the anonymous referee for a careful reading and constructive comments. This scientific work makes use of the Murchison Radio-astronomy Observatory (MRO), operated by the Commonwealth Scientific and Industrial Research Organisation (CSIRO). We acknowledge the Wajarri Yamatji people as the traditional owners of the Observatory site. Support for the operation of the MWA is provided by the Australian Government’s National Collaborative Research Infrastructure Strategy (NCRIS), under a contract to Curtin University administered by Astronomy Australia Limited. We acknowledge the Pawsey Supercomputing Centre, which is supported by the Western Australian and Australian Governments. The SDO is a National Aeronautics and Space Administration (NASA) satellite, and we acknowledge the AIA and HMI science teams for providing open access to data and software. This research has also made use of NASA’s Astrophysics Data System (ADS) and the Virtual Solar Observatory (VSO, Hill *et al.* 2009).

References

- Akhmedov, S.B., Gelfreikh, G.B., Bogod, V.M., Korzhavin, A.N.: 1982, The measurement of magnetic fields in the solar atmosphere above sunspots using gyroresonance emission. *Solar Phys.* **79**, 41. [DOI](#). [ADS](#).
- Alissandrakis, C.E.: 1994, Radio observations of the quiet solar corona. *Advances in Space Research* **14**. [DOI](#). [ADS](#).
- Alissandrakis, C.E., Lantos, P., Nicolaidis, E.: 1985, Coronal structures observed at metric wavelengths with the Nancay radioheliograph. *Solar Phys.* **97**, 267. [DOI](#). [ADS](#).
- Altyntsev, A., Meshalkina, N., Myshyakov, I., Pal’shin, V., Fleishman, G.: 2017, Flare SOL2012-07-06: On the Origin of the Circular Polarization Reversal Between 17 GHz and 34 GHz. *Solar Phys.* **292**, 137. [DOI](#). [ADS](#).
- Aschwanden, M.J.: 1986, The polarization of decimetric pulsations. *Solar Phys.* **104**, 57. [DOI](#). [ADS](#).
- Aschwanden, M.J.: 2005, *Physics of the Solar Corona. An Introduction with Problems and Solutions (2nd edition)*. [ADS](#).

- Benkevitch, L.V., Oberoi, D., Benjamin, M.D., Sokolov, I.V.: 2012, HART: An Efficient Modeling Framework for Simulated Solar Imaging. In: Ballester, P., Egret, D., Lorente, N.P.F. (eds.) *Astronomical Data Analysis Software and Systems XXI*, *Astronomical Society of the Pacific Conference Series* **461**, 475. [ADS](#).
- Bentley, R.D., Klein, K.-L., van Driel-Gesztelyi, L., Démoulin, P., Trottet, G., Tassetto, P., Marty, G.: 2000, Magnetic Activity Associated With Radio Noise Storms. *Solar Phys.* **193**, 227. [DOI](#). [ADS](#).
- Benz, A.O., Wentzel, D.G.: 1981, Coronal evolution and solar type I radio bursts - an ion-acoustic wave model. *Astron. Astrophys.* **94**, 100. [ADS](#).
- Bouratzis, C., Hillaris, A., Alissandrakis, C.E., Preka-Papadema, P., Moussas, X., Caroubalos, C., Tsitsipis, P., Kontogeorgos, A.: 2016, High resolution observations with Artemis-IV and the NRH. I. Type IV associated narrow-band bursts. *Astron. Astrophys.* **586**, A29. [DOI](#). [ADS](#).
- Bowman, J.D., Cairns, I., Kaplan, D.L., Murphy, T., Oberoi, D., Staveley-Smith, L., Arcus, W., Barnes, D.G., Bernardi, G., Briggs, F.H., Brown, S., Bunton, J.D., Burgasser, A.J., Cappallo, R.J., Chatterjee, S., Corey, B.E., Coster, A., Deshpande, A., deSouza, L., Emrich, D., Erickson, P., Goeke, R.F., Gaensler, B.M., Greenhill, L.J., Harvey-Smith, L., Hazelton, B.J., Herne, D., Hewitt, J.N., Johnston-Hollitt, M., Kasper, J.C., Kincaid, B.B., Koenig, R., Kratzenberg, E., Lonsdale, C.J., Lynch, M.J., Matthews, L.D., McWhirter, S.R., Mitchell, D.A., Morales, M.F., Morgan, E.H., Ord, S.M., Pathikulangara, J., Prabu, T., Remillard, R.A., Robishaw, T., Rogers, A.E.E., Roshi, A.A., Salah, J.E., Sault, R.J., Shankar, N.U., Srivani, K.S., Stevens, J.B., Subrahmanyam, R., Tingay, S.J., Wayth, R.B., Waterson, M., Webster, R.L., Whitney, A.R., Williams, A.J., Williams, C.L., Wyithe, J.S.B.: 2013, Science with the Murchison Widefield Array. *PASA* **30**, e031. [DOI](#). [ADS](#).
- Briggs, D.S.: 1995, High Fidelity Interferometric Imaging: Robust Weighting and NNLS Deconvolution. In: *American Astronomical Society Meeting Abstracts*, *Bulletin of the American Astronomical Society* **27**, 1444. [ADS](#).
- Butterworth, S.: 1930, On the theory of filter amplifiers. *Wireless Engineer* **7**(6), 536.
- Cairns, I.H., Knock, S.A., Robinson, P.A., Kuncic, Z.: 2003, Type II Solar Radio Bursts: Theory and Space Weather Implications. *Space Sci. Rev.* **107**, 27. [DOI](#). [ADS](#).
- Cairns, I.H., Lobzin, V.V., Donea, A., Tingay, S.J., McCauley, P.I., Oberoi, D., Duffin, R.T., Reiner, M.J., Hurley-Walker, N., Kudryavtseva, N.A., Melrose, D.B., Harding, J.C., Bernardi, G., Bowman, J.D., Cappallo, R.J., Corey, B.E., Deshpande, A., Emrich, D., Goeke, R., Hazelton, B.J., Johnston-Hollitt, M., Kaplan, D.L., Kasper, J.C., Kratzenberg, E., Lonsdale, C.J., Lynch, M.J., McWhirter, S.R., Mitchell, D.A., Morales, M.F., Morgan, E., Ord, S.M., Prabu, T., Roshi, A., Shankar, N.U., Srivani, K.S., Subrahmanyam, R., Wayth, R.B., Waterson, M., Webster, R.L., Whitney, A.R., Williams, A., Williams, C.L.: 2018, Low Altitude Solar Magnetic Reconnection, Type III Solar Radio Bursts, and X-ray Emissions. *Scientific Reports* **8**, 1676. [DOI](#). [ADS](#).
- Cohen, M.H.: 1960, Magnetoionic Mode Coupling at High Frequencies. *Astrophys. J.* **131**, 664. [DOI](#). [ADS](#).
- Cranmer, S.R.: 2009, Coronal Holes. *Living Reviews in Solar Physics* **6**, 3. [DOI](#). [ADS](#).
- Cranmer, S.R., Woolsey, L.N.: 2015, Driving Solar Spicules and Jets with Magnetohydrodynamic Turbulence: Testing a Persistent Idea. *Astrophys. J.* **812**, 71. [DOI](#). [ADS](#).
- De Pontieu, B., Martínez-Sykora, J., Chintzoglou, G.: 2017, What Causes the High Apparent Speeds in Chromospheric and Transition Region Spicules on the Sun? *Astrophys. J. Lett.* **849**, L7. [DOI](#). [ADS](#).
- Del Zanna, G., Aulanier, G., Klein, K.-L., Török, T.: 2011, A single picture for solar coronal outflows and radio noise storms. *Astron. Astrophys.* **526**, A137. [DOI](#). [ADS](#).
- Dulk, G.A.: 1985, Radio emission from the sun and stars. *Ann. Rev. Astron. Astrophys.* **23**, 169. [DOI](#). [ADS](#).
- Dulk, G.A., McLean, D.J.: 1978, Coronal magnetic fields. *Solar Phys.* **57**, 279. [DOI](#). [ADS](#).
- Dulk, G.A., Sheridan, K.V.: 1974, The Structure of the Middle Corona from Observations at 80 and 160 MHz. *Solar Phys.* **36**, 191. [DOI](#). [ADS](#).
- Dulk, G.A., Suzuki, S., Sheridan, K.V.: 1984, Solar noise storms - The polarization of storm Type III and related bursts. *Astron. Astrophys.* **130**, 39. [ADS](#).
- Elgarøy, E.Ø.: 1977, *Solar noise storms*. [ADS](#).
- Freeland, S.L., Handy, B.N.: 1998, Data Analysis with the SolarSoft System. *Solar Phys.* **182**, 497. [DOI](#).

ADS.

- Gelfreikh, G.B.: 2004, Coronal Magnetic Field Measurements Through Bremsstrahlung Emission. In: Gary, D.E., Keller, C.U. (eds.) *Astrophysics and Space Science Library, Astrophysics and Space Science Library* **314**, 115. DOI. ADS.
- Gergely, T.E., Erickson, W.C.: 1975, Decameter storm radiation. I. *Solar Phys.* **42**, 467. DOI. ADS.
- Gibson, S., Kucera, T., White, S., Dove, J., Fan, Y., Forland, B., Rachmeler, L., Downs, C., Reeves, K.: 2016, FORWARD: A toolset for multiwavelength coronal magnetometry. *Frontiers in Astronomy and Space Sciences* **3**, 8. DOI. ADS.
- Ginzburg, V.L., Zhelezniakov, V.V.: 1958, On the Possible Mechanisms of Sporadic Solar Radio Emission (Radiation in an Isotropic Plasma). *Soviet Astron.* **2**, 653. ADS.
- Gopalswamy, N., Kundu, M.R., Raoult, A., Pick, M.: 1994, Non-radial magnetic field structures in the solar corona. *Solar Phys.* **150**, 317. DOI. ADS.
- Grebinskij, A., Bogod, V., Gelfreikh, G., Urpo, S., Pohjolainen, S., Shibasaki, K.: 2000, Microwave tomography of solar magnetic fields. *Astron. Astrophys. Suppl.* **144**, 169. DOI. ADS.
- Hariharan, K., Ramesh, R., Kathiravan, C.: 2015, Observations of Near-Simultaneous Split-Band Solar Type-II Radio Bursts at Low Frequencies. *Solar Phys.* **290**, 2479. DOI. ADS.
- Hariharan, K., Ramesh, R., Kishore, P., Kathiravan, C., Gopalswamy, N.: 2014, An Estimate of the Coronal Magnetic Field near a Solar Coronal Mass Ejection from Low-frequency Radio Observations. *Astrophys. J.* **795**, 14. DOI. ADS.
- Hariharan, K., Ramesh, R., Kathiravan, C., Wang, T.J.: 2016, Simultaneous Near-Sun Observations of a Moving Type IV Radio Burst and the Associated White-Light Coronal Mass Ejection. *Solar Phys.* **291**, 1405. DOI. ADS.
- Hill, F., Martens, P., Yoshimura, K., Gurman, J., Hourclé, J., Dimitoglou, G., Suárez-Solá, I., Wampler, S., Reardon, K., Davey, A., Bogart, R.S., Tian, K.Q.: 2009, The Virtual Solar Observatory—A Resource for International Heliophysics Research. *Earth Moon and Planets* **104**, 315. DOI. ADS.
- Hurley-Walker, N., Morgan, J., Wayth, R.B., Hancock, P.J., Bell, M.E., Bernardi, G., Bhat, R., Briggs, F., Deshpande, A.A., Ewall-Wice, A., Feng, L., Hazelton, B.J., Hindson, L., Jacobs, D.C., Kaplan, D.L., Kudryavtseva, N., Lenc, E., McKinley, B., Mitchell, D., Pindor, B., Procopio, P., Oberoi, D., Offringa, A., Ord, S., Riding, J., Bowman, J.D., Cappallo, R., Corey, B., Emrich, D., Gaensler, B.M., Goeke, R., Greenhill, L., Hewitt, J., Johnston-Hollitt, M., Kasper, J., Kratzenberg, E., Lonsdale, C., Lynch, M., McWhirter, R., Morales, M.F., Morgan, E., Prabu, T., Rogers, A., Roshi, A., Shankar, U., Srivani, K., Subrahmanyam, R., Tingay, S., Waterson, M., Webster, R., Whitney, A., Williams, A., Williams, C.: 2014, The Murchison Widefield Array Commissioning Survey: A Low-Frequency Catalogue of 14 110 Compact Radio Sources over 6 100 Square Degrees. *PASA* **31**, e045. DOI. ADS.
- Hurley-Walker, N., Callingham, J.R., Hancock, P.J., Franzen, T.M.O., Hindson, L., Kapińska, A.D., Morgan, J., Offringa, A.R., Wayth, R.B., Wu, C., Zheng, Q., Murphy, T., Bell, M.E., Dwarakanath, K.S., For, B., Gaensler, B.M., Johnston-Hollitt, M., Lenc, E., Procopio, P., Staveley-Smith, L., Ekers, R., Bowman, J.D., Briggs, F., Cappallo, R.J., Deshpande, A.A., Greenhill, L., Hazelton, B.J., Kaplan, D.L., Lonsdale, C.J., McWhirter, S.R., Mitchell, D.A., Morales, M.F., Morgan, E., Oberoi, D., Ord, S.M., Prabu, T., Shankar, N.U., Srivani, K.S., Subrahmanyam, R., Tingay, S.J., Webster, R.L., Williams, A., Williams, C.L.: 2017, GaLactic and Extragalactic All-sky Murchison Widefield Array (GLEAM) survey - I. A low-frequency extragalactic catalogue. *Mon. Not. Roy. Astron. Soc.* **464**, 1146. DOI. ADS.
- IAU: 1973, Commission 40: Radio astronomy (radio astronomie). *Transactions of the International Astronomical Union* **15**(2), 165?167. DOI.
- IEEE: 1969, Ieee standard definitions of terms for radio wave propagation. *IEEE Transactions on Antennas and Propagation* **17**(3), 270. DOI.
- Iwai, K., Misawa, H., Tsuchiya, F., Morioka, A., Masuda, S., Miyoshi, Y.: 2012, Survey of Accelerated Particles in a Solar Active Region Using Hinode/XRT and Ground-Based Type-I Radio Burst Observations. In: Sekii, T., Watanabe, T., Sakurai, T. (eds.) *Hinode-3: The 3rd Hinode Science Meeting, Astronomical Society of the Pacific Conference Series* **454**, 249. ADS.
- Kai, K.: 1962, Some Characteristics of Type I Burst. *Pub. Astron. Soc. Japan* **14**, 1. ADS.
- Kaneda, K., Misawa, H., Iwai, K., Tsuchiya, F., Obara, T.: 2015, Frequency Dependence of Polarization

- of Zebra Pattern in Type-IV Solar Radio Bursts. *Astrophys. J. Lett.* **808**, L45. DOI. ADS.
- Kaneda, K., Misawa, H., Iwai, K., Tsuchiya, F., Obara, T., Katoh, Y., Masuda, S.: 2017, Polarization Characteristics of Zebra Patterns in Type IV Solar Radio Bursts. *Astrophys. J.* **842**, 45. DOI. ADS.
- Kaplan, D.L., Tingay, S.J., Manoharan, P.K., Macquart, J.P., Hancock, P., Morgan, J., Mitchell, D.A., Ekers, R.D., Wayth, R.B., Trott, C., Murphy, T., Oberoi, D., Cairns, I.H., Feng, L., Kudryavtseva, N., Bernardi, G., Bowman, J.D., Briggs, F., Cappallo, R.J., Deshpande, A.A., Gaensler, B.M., Greenhill, L.J., Hurley Walker, N., Hazelton, B.J., Johnston Hollitt, M., Lonsdale, C.J., McWhirter, S.R., Morales, M.F., Morgan, E., Ord, S.M., Prabu, T., Udaya Shankar, N., Srivani, K.S., Subrahmanyam, R., Webster, R.L., Williams, A., Williams, C.L.: 2015, Murchison Widefield Array Observations of Anomalous Variability: A Serendipitous Night-time Detection of Interplanetary Scintillation. *Astrophys. J. Lett.* **809**, L12. DOI. ADS.
- Kayshap, P., Murawski, K., Srivastava, A.K., Dwivedi, B.N.: 2018, Rotating network jets in the quiet Sun as observed by IRIS. *Astron. Astrophys.* **616**, A99. DOI. ADS.
- Kerdraon, A., Delouis, J.-M.: 1997, The Nançay Radioheliograph. In: Trotter, G. (ed.) *Coronal Physics from Radio and Space Observations, Lecture Notes in Physics, Berlin Springer Verlag* **483**, 192. DOI. ADS.
- Kishore, P., Ramesh, R., Kathiravan, C., Rajalingam, M.: 2015, A Low-Frequency Radio Spectropolarimeter for Observations of the Solar Corona. *Solar Phys.* **290**, 2409. DOI. ADS.
- Kishore, P., Kathiravan, C., Ramesh, R., Ebenezer, E.: 2017, Coronal Magnetic Field Lines and Electrons Associated with Type III-V Radio Bursts in a Solar Flare. *Journal of Astrophysics and Astronomy* **38**, 24. DOI. ADS.
- Klein, K.-L.: 1998, Suprathermal Electrons in Non-flaring Active Regions (Invited review). In: Alissandrakis, C.E., Schmieder, B. (eds.) *Three-Dimensional Structure of Solar Active Regions, Astronomical Society of the Pacific Conference Series* **155**, 182. ADS.
- Kong, X., Chen, Y., Feng, S., Du, G., Li, C., Koval, A., Vasanth, V., Wang, B., Guo, F., Li, G.: 2016, Observation of a Metric Type N Solar Radio Burst. *Astrophys. J.* **830**, 37. DOI. ADS.
- Kumari, A., Ramesh, R., Kathiravan, C., Wang, T.J.: 2017, Strength of the Solar Coronal Magnetic Field - A Comparison of Independent Estimates Using Contemporaneous Radio and White-Light Observations. *Solar Phys.* **292**, 161. DOI. ADS.
- Lantos, P.: 1999, Low Frequency Observations of the Quiet Sun: a Review. In: Bastian, T.S., Gopalswamy, N., Shibasaki, K. (eds.) *Proceedings of the Nobeyama Symposium* **479**, 11. ADS.
- Lantos, P., Alissandrakis, C.E., Gergely, T., Kundu, M.R.: 1987, Quiet sun and slowly varying component at meter and decameter wavelengths. *Solar Phys.* **112**, 325. DOI. ADS.
- Le Squeren, A.M.: 1963, Étude des orages radioélectriques solaires sur 169 MHz à l'aide de l'interféromètre en croix de la station de Nançay. *Annales d'Astrophysique* **26**, 97. ADS.
- Lemen, J.R., Title, A.M., Akin, D.J., Boerner, P.F., Chou, C., Drake, J.F., Duncan, D.W., Edwards, C.G., Friedlaender, F.M., Heyman, G.F., Hurlburt, N.E., Katz, N.L., Kushner, G.D., Levay, M., Lindgren, R.W., Mathur, D.P., McFeaters, E.L., Mitchell, S., Rehse, R.A., Schrijver, C.J., Springer, L.A., Stern, R.A., Tarbell, T.D., Wuelser, J.-P., Wolfson, C.J., Yanari, C., Bookbinder, J.A., Cheimets, P.N., Caldwell, D., Deluca, E.E., Gates, R., Golub, L., Park, S., Podgorski, W.A., Bush, R.I., Scherrer, P.H., Gummin, M.A., Smith, P., Auken, G., Jerram, P., Pool, P., Soufli, R., Windt, D.L., Beardsley, S., Clapp, M., Lang, J., Waltham, N.: 2012, The Atmospheric Imaging Assembly (AIA) on the Solar Dynamics Observatory (SDO). *Solar Phys.* **275**, 17. DOI. ADS.
- Lenc, E., Anderson, C.S., Barry, N., Bowman, J.D., Cairns, I.H., Farnes, J.S., Gaensler, B.M., Heald, G., Johnston-Hollitt, M., Kaplan, D.L., Lynch, C.R., McCauley, P.I., Mitchell, D.A., Morgan, J., Morales, M.F., Murphy, T., Offringa, A.R., Ord, S.M., Pindor, B., Riseley, C., Sadler, E.M., Sobey, C., Sokolowski, M., Sullivan, I.S., O'Sullivan, S.P., Sun, X.H., Tremblay, S.E., Trott, C.M., Wayth, R.B.: 2017, The Challenges of Low-Frequency Radio Polarimetry: Lessons from the Murchison Widefield Array. *Pub. Astron. Soc. Austral.* **34**, e040. DOI. ADS.
- Lenc, E., Murphy, T., Lynch, C.R., Kaplan, D.L., Zhang, S.N.: 2018, An all-sky survey of circular polarization at 200 MHz. *Mon. Not. Roy. Astron. Soc.* **478**, 2835. DOI. ADS.
- Li, C.Y., Chen, Y., Wang, B., Ruan, G.P., Feng, S.W., Du, G.H., Kong, X.L.: 2017, EUV and Magnetic

- Activities Associated with Type-I Solar Radio Bursts. *Solar Phys.* **292**, 82. DOI. ADS.
- Lionello, R., Linker, J.A., Mikić, Z.: 2009, Multispectral Emission of the Sun During the First Whole Sun Month: Magnetohydrodynamic Simulations. *Astrophys. J.* **690**, 902. DOI. ADS.
- Liu, H., Chen, Y., Cho, K., Feng, S., Vasanth, V., Koval, A., Du, G., Wu, Z., Li, C.: 2018, A Solar Stationary Type IV Radio Burst and Its Radiation Mechanism. *Solar Phys.* **293**, 58. DOI. ADS.
- Lonsdale, C.J., Cappallo, R.J., Morales, M.F., Briggs, F.H., Benkevitch, L., Bowman, J.D., Bunton, J.D., Burns, S., Corey, B.E., Desouza, L., Doeleman, S.S., Derome, M., Deshpande, A., Gopala, M.R., Greenhill, L.J., Herne, D.E., Hewitt, J.N., Kamini, P.A., Kasper, J.C., Kincaid, B.B., Kocz, J., Kowald, E., Kratzenberg, E., Kumar, D., Lynch, M.J., Madhavi, S., Matejek, M., Mitchell, D.A., Morgan, E., Oberoi, D., Ord, S., Pathikulangara, J., Prabu, T., Rogers, A., Roshi, A., Salah, J.E., Sault, R.J., Shankar, N.U., Srivani, K.S., Stevens, J., Tingay, S., Vaccarella, A., Waterson, M., Wayth, R.B., Webster, R.L., Whitney, A.R., Williams, A., Williams, C.: 2009, The Murchison Widefield Array: Design Overview. *IEEE Proceedings* **97**, 1497. DOI. ADS.
- Mandrini, C.H., Baker, D., Démoulin, P., Cristiani, G.D., van Driel-Gesztelyi, L., Vargas Domínguez, S., Nuevo, F.A., Vásquez, A.M., Pick, M.: 2015, Parallel Evolution of Quasi-separatrix Layers and Active Region Upflows. *Astrophys. J.* **809**, 73. DOI. ADS.
- McCauley, P.I., Cairns, I.H., Morgan, J.: 2018, Densities Probed by Coronal Type III Radio Burst Imaging. *Solar Phys.* **293**, 132. DOI. ADS.
- McCauley, P.I., Cairns, I.H., Morgan, J., Gibson, S.E., Harding, J.C., Lonsdale, C., Oberoi, D.: 2017, Type III Solar Radio Burst Source Region Splitting due to a Quasi-separatrix Layer. *Astrophys. J.* **851**, 151. DOI. ADS.
- Melrose, D.B.: 1980, *Plasma astrophysics. Nonthermal processes in diffuse magnetized plasmas - Vol.1: The emission, absorption and transfer of waves in plasmas; Vol.2: Astrophysical applications.* ADS.
- Melrose, D.B.: 1986, *Instabilities in space and laboratory plasmas.* ADS.
- Melrose, D.B.: 1989, Depolarization of solar bursts due to scattering by low-frequency waves. *Solar Phys.* **119**, 143. DOI. ADS.
- Melrose, D.B.: 2006, Depolarization of Radio Bursts Due to Reflection off Sharp Boundaries in the Solar Corona. *Astrophys. J.* **637**, 1113. DOI. ADS.
- Melrose, D.B.: 2009, Coherent emission. In: Gopalswamy, N., Webb, D.F. (eds.) *Universal Heliophysical Processes, IAU Symposium* **257**, 305. DOI. ADS.
- Melrose, D.B., Robinson, P.A.: 1994, Reversal of the sense of polarisation in solar and stellar radio flares. *Proceedings of the Astronomical Society of Australia* **11**, 16. ADS.
- Melrose, D.B., Dulk, G.A., Smerd, S.F.: 1978, The polarization of second harmonic plasma emission. *Astron. Astrophys.* **66**, 315. ADS.
- Mercier, C.: 1990, Polarisation of type III bursts between 164 and 435 MHz - Structure and variation with frequency. *Solar Phys.* **130**, 119. DOI. ADS.
- Mohan, A., Oberoi, D.: 2017, 4D Data Cubes from Radio-Interferometric Spectroscopic Snapshot Imaging. *Solar Phys.* **292**, 168. DOI. ADS.
- Mohan, A., Mondal, S., Oberoi, D., Lonsdale, C.: 2018, Evidence for Super-Alfvénic oscillations in sources of Solar type III radio bursts. *arXiv e-prints.* ADS.
- Mohan, A., McCauley, P.I., Mastrano, A., Oberoi, D.: 2019, A weak coronal heating event associated with periodic particle acceleration episodes. *arXiv e-prints.* ADS.
- Mondal, S., Mohan, A., Oberoi, D., Morgan, J.S., Benkevitch, L., Lonsdale, C.J., Crowley, M., Cairns, I.H.: 2019, Unsupervised generation of high dynamic range solar images: A novel algorithm for self-calibration of interferometry data. *arXiv e-prints.* ADS.
- Morgan, J.S., Macquart, J.-P., Ekers, R., Chhetri, R., Tokumaru, M., Manoharan, P.K., Tremblay, S., Bisi, M.M., Jackson, B.V.: 2018, Interplanetary Scintillation with the Murchison Widefield Array I: a sub-arcsecond survey over 900 deg² at 79 and 158 MHz. *Mon. Not. Roy. Astron. Soc.* **473**, 2965. DOI. ADS.
- Mugundhan, V., Ramesh, R., Kathiravan, C., Gireesh, G.V.S., Hegde, A.: 2018, Spectropolarimetric Observations of Solar Noise Storms at Low Frequencies. *Solar Phys.* **293**, 41. DOI. ADS.
- Narang, N., Arbacher, R.T., Tian, H., Banerjee, D., Cranmer, S.R., DeLuca, E.E., McKillop, S.: 2016,

- Statistical Study of Network Jets Observed in the Solar Transition Region: a Comparison Between Coronal Holes and Quiet-Sun Regions. *Solar Phys.* **291**, 1129. DOI. ADS.
- Newkirk, G. Jr.: 1961, The Solar Corona in Active Regions and the Thermal Origin of the Slowly Varying Component of Solar Radio Radiation. *Astrophys. J.* **133**, 983. DOI. ADS.
- Oberoi, D., Sharma, R., Rogers, A.E.E.: 2017, Estimating Solar Flux Density at Low Radio Frequencies Using a Sky Brightness Model. *Solar Phys.* **292**, 75. DOI. ADS.
- Offringa, A.R., van de Gronde, J.J., Roerdink, J.B.T.M.: 2012, A morphological algorithm for improving radio-frequency interference detection. *Astron. Astrophys.* **539**, A95. DOI. ADS.
- Offringa, A.R., McKinley, B., Hurley-Walker, N., Briggs, F.H., Wayth, R.B., Kaplan, D.L., Bell, M.E., Feng, L., Neben, A.R., Hughes, J.D., Rhee, J., Murphy, T., Bhat, N.D.R., Bernardi, G., Bowman, J.D., Cappallo, R.J., Corey, B.E., Deshpande, A.A., Emrich, D., Ewall-Wice, A., Gaensler, B.M., Goeke, R., Greenhill, L.J., Hazelton, B.J., Hindson, L., Johnston-Hollitt, M., Jacobs, D.C., Kasper, J.C., Kratzenberg, E., Lenc, E., Lonsdale, C.J., Lynch, M.J., McWhirter, S.R., Mitchell, D.A., Morales, M.F., Morgan, E., Kudryavtseva, N., Oberoi, D., Ord, S.M., Pindor, B., Procopio, P., Prabu, T., Riding, J., Roshi, D.A., Shankar, N.U., Srivani, K.S., Subrahmanyam, R., Tingay, S.J., Waterson, M., Webster, R.L., Whitney, A.R., Williams, A., Williams, C.L.: 2014, WSCLEAN: an implementation of a fast, generic wide-field imager for radio astronomy. *Mon. Not. Roy. Astron. Soc.* **444**, 606. DOI. ADS.
- Offringa, A.R., Wayth, R.B., Hurley-Walker, N., Kaplan, D.L., Barry, N., Beardsley, A.P., Bell, M.E., Bernardi, G., Bowman, J.D., Briggs, F., Callingham, J.R., Cappallo, R.J., Carroll, P., Deshpande, A.A., Dillon, J.S., Dwarakanath, K.S., Ewall-Wice, A., Feng, L., For, B.-Q., Gaensler, B.M., Greenhill, L.J., Hancock, P., Hazelton, B.J., Hewitt, J.N., Hindson, L., Jacobs, D.C., Johnston-Hollitt, M., Kapińska, A.D., Kim, H.-S., Kittiwisit, P., Lenc, E., Line, J., Loeb, A., Lonsdale, C.J., McKinley, B., McWhirter, S.R., Mitchell, D.A., Morales, M.F., Morgan, E., Morgan, J., Neben, A.R., Oberoi, D., Ord, S.M., Paul, S., Pindor, B., Pober, J.C., Prabu, T., Procopio, P., Riding, J., Udaya Shankar, N., Sethi, S., Srivani, K.S., Staveley-Smith, L., Subrahmanyam, R., Sullivan, I.S., Tegmark, M., Thyagarajan, N., Tingay, S.J., Trott, C.M., Webster, R.L., Williams, A., Williams, C.L., Wu, C., Wyithe, J.S., Zheng, Q.: 2015, The Low-Frequency Environment of the Murchison Widefield Array: Radio-Frequency Interference Analysis and Mitigation. *PASA* **32**, e008. DOI. ADS.
- Ord, S.M., Crosse, B., Emrich, D., Pallot, D., Wayth, R.B., Clark, M.A., Tremblay, S.E., Arcus, W., Barnes, D., Bell, M., Bernardi, G., Bhat, N.D.R., Bowman, J.D., Briggs, F., Bunton, J.D., Cappallo, R.J., Corey, B.E., Deshpande, A.A., deSouza, L., Ewall-Wice, A., Feng, L., Goeke, R., Greenhill, L.J., Hazelton, B.J., Herne, D., Hewitt, J.N., Hindson, L., Hurley-Walker, N., Jacobs, D., Johnston-Hollitt, M., Kaplan, D.L., Kasper, J.C., Kincaid, B.B., Koenig, R., Kratzenberg, E., Kudryavtseva, N., Lenc, E., Lonsdale, C.J., Lynch, M.J., McKinley, B., McWhirter, S.R., Mitchell, D.A., Morales, M.F., Morgan, E., Oberoi, D., Offringa, A., Pathikulangara, J., Pindor, B., Prabu, T., Procopio, P., Remillard, R.A., Riding, J., Rogers, A.E.E., Roshi, A., Salah, J.E., Sault, R.J., Udaya Shankar, N., Srivani, K.S., Stevens, J., Subrahmanyam, R., Tingay, S.J., Waterson, M., Webster, R.L., Whitney, A.R., Williams, A., Williams, C.L., Wyithe, J.S.B.: 2015, The Murchison Widefield Array Correlator. *PASA* **32**, e006. DOI. ADS.
- Pesnell, W.D., Thompson, B.J., Chamberlin, P.C.: 2012, The Solar Dynamics Observatory (SDO). *Solar Phys.* **275**, 3. DOI. ADS.
- Rahman, M.M., McCauley, P.I., Cairns, I.H.: 2019, On the Relative Brightness of Coronal Holes at Low Frequencies. *Solar Phys.* **294**, 7. DOI. ADS.
- Ramesh, R., Kathiravan, C., Narayanan, A.S.: 2011, Low-frequency Observations of Polarized Emission from Long-lived Non-thermal Radio Sources in the Solar Corona. *Astrophys. J.* **734**, 39. DOI. ADS.
- Ramesh, R., Kathiravan, C., Sastry, C.V.: 2010, Estimation of Magnetic Field in the Solar Coronal Streamers Through Low Frequency Radio Observations. *Astrophys. J.* **711**, 1029. DOI. ADS.
- Ramesh, R., Subramanian, K.R., Sundararajan, M.S., Sastry, C.V.: 1998, The Gauribidanur Radioheliograph. *Solar Phys.* **181**, 439. DOI. ADS.
- Ramesh, R., Kathiravan, C., Sundararajan, M.S., Barve, I.V., Sastry, C.V.: 2008, A Low-Frequency (30 - 110 MHz) Antenna System for Observations of Polarized Radio Emission from the Solar Corona. *Solar Phys.* **253**, 319. DOI. ADS.
- Ramesh, R., Kathiravan, C., Barve, I.V., Beeharry, G.K., Rajasekara, G.N.: 2010, Radio Observations of

- Weak Energy Releases in the Solar Corona. *Astrophys. J. Lett.* **719**, L41. DOI. ADS.
- Ramesh, R., Sasikumar Raja, K., Kathiravan, C., Narayanan, A.S.: 2013, Low-frequency Radio Observations of Picoflare Category Energy Releases in the Solar Atmosphere. *Astrophys. J.* **762**, 89. DOI. ADS.
- Reid, H.A.S., Ratcliffe, H.: 2014, A review of solar type III radio bursts. *Research in Astronomy and Astrophysics* **14**, 773. DOI. ADS.
- Robinson, P.A., Cairns, I.H.: 2000, Theory of Type III And Type II Solar Radio Emissions. *Washington DC American Geophysical Union Geophysical Monograph Series* **119**, 37. DOI. ADS.
- Ryabov, B.: 2004, Coronal Magnetic Field Measurements Through Quasi-Transverse Propagation. In: Gary, D.E., Keller, C.U. (eds.) *Astrophysics and Space Science Library, Astrophysics and Space Science Library* **314**, 135. DOI. ADS.
- Ryabov, B.I., Pilyeva, N.A., Alissandrakis, C.E., Shibasaki, K., Bogod, V.M., Garaimov, V.I., Gelfreikh, G.B.: 1999, Coronal Magnetography of an Active Region From Microwave Polarization Inversion. *Solar Phys.* **185**, 157. DOI. ADS.
- Saito, K., Poland, A.I., Munro, R.H.: 1977, A study of the background corona near solar minimum. *Solar Phys.* **55**, 121. DOI. ADS.
- Sasikumar Raja, K., Ramesh, R.: 2013, Low-frequency Observations of Transient Quasi-periodic Radio Emission from the Solar Atmosphere. *Astrophys. J.* **775**, 38. DOI. ADS.
- Sasikumar Raja, K., Kathiravan, C., Ramesh, R., Rajalingam, M., Barve, I.V.: 2013, Design and Performance of a Low-frequency Cross-polarized Log-periodic Dipole Antenna. *Astrophys. J. Supp.* **207**, 2. DOI. ADS.
- Sasikumar Raja, K., Ramesh, R., Hariharan, K., Kathiravan, C., Wang, T.J.: 2014, An Estimate of the Magnetic Field Strength Associated with a Solar Coronal Mass Ejection from Low Frequency Radio Observations. *Astrophys. J.* **796**, 56. DOI. ADS.
- Sastry, C.V.: 2009, Polarization of the Thermal Radio Emission from Outer Solar Corona. *Astrophys. J.* **697**, 1934. DOI. ADS.
- Scherrer, P.H., Schou, J., Bush, R.I., Kosovichev, A.G., Bogart, R.S., Hoeksema, J.T., Liu, Y., Duvall, T.L., Zhao, J., Title, A.M., Schrijver, C.J., Tarbell, T.D., Tomczyk, S.: 2012, The Helioseismic and Magnetic Imager (HMI) Investigation for the Solar Dynamics Observatory (SDO). *Solar Phys.* **275**, 207. DOI. ADS.
- Schrijver, C.J., De Rosa, M.L.: 2003, Photospheric and heliospheric magnetic fields. *Solar Phys.* **212**, 165. DOI. ADS.
- Shain, A.V., Melnikov, V.F., Morgachev, A.S.: 2017, The Role of Quasi-Transverse Propagation in Observed Polarization of Flare Loop Microwave Radiation. *Geomagnetism and Aeronomy* **57**, 988. DOI. ADS.
- Sharma, R., Oberoi, D., Arjunwadkar, M.: 2018, Quantifying Weak Nonthermal Solar Radio Emission at Low Radio Frequencies. *Astrophys. J.* **852**, 69. DOI. ADS.
- Sharykin, I.N., Kuznetsov, A.A., Myshyakov, I.I.: 2018, Probing Twisted Magnetic Field Using Microwave Observations in an M Class Solar Flare on 11 February, 2014. *Solar Phys.* **293**, 34. DOI. ADS.
- Shibasaki, K., Alissandrakis, C.E., Pohjolainen, S.: 2011, Radio Emission of the Quiet Sun and Active Regions (Invited Review). *Solar Phys.* **273**, 309. DOI. ADS.
- Spicer, D.S., Benz, A.O., Huba, J.D.: 1982, Solar type I noise storms and newly emerging magnetic flux. *Astron. Astrophys.* **105**, 221. ADS.
- Suresh, A., Sharma, R., Oberoi, D., Das, S.B., Pankratius, V., Timar, B., Lonsdale, C.J., Bowman, J.D., Briggs, F., Cappallo, R.J., Corey, B.E., Deshpande, A.A., Emrich, D., Goeke, R., Greenhill, L.J., Hazelton, B.J., Johnston-Hollitt, M., Kaplan, D.L., Kasper, J.C., Kratzenberg, E., Lynch, M.J., McWhirter, S.R., Mitchell, D.A., Morales, M.F., Morgan, E., Ord, S.M., Prabu, T., Rogers, A.E.E., Roshi, A., Udaya Shankar, N., Srivani, K.S., Subrahmanyam, R., Tingay, S.J., Waterson, M., Wayth, R.B., Webster, R.L., Whitney, A.R., Williams, A., Williams, C.L.: 2017, Wavelet-based Characterization of Small-scale Solar Emission Features at Low Radio Frequencies. *Astrophys. J.* **843**, 19. DOI. ADS.
- Sutinjo, A., O'Sullivan, J., Lenc, E., Wayth, R.B., Padhi, S., Hall, P., Tingay, S.J.: 2015, Understanding instrumental Stokes leakage in Murchison Widefield Array polarimetry. *Radio Science* **50**, 52. DOI.

ADS.

- Suzuki, S., Sheridan, K.V.: 1980, The polarization of metre-wave solar emission. *Proceedings of the Astronomical Society of Australia* **4**, 56. DOI. ADS.
- Tian, H., DeLuca, E.E., Cranmer, S.R., De Pontieu, B., Peter, H., Martínez-Sykora, J., Golub, L., McKillop, S., Reeves, K.K., Miralles, M.P., McCauley, P., Saar, S., Testa, P., Weber, M., Murphy, N., Lemen, J., Title, A., Boerner, P., Hurlburt, N., Tarbell, T.D., Wuelsel, J.P., Kleint, L., Kankelborg, C., Jaeggli, S., Carlsson, M., Hansteen, V., McIntosh, S.W.: 2014, Prevalence of small-scale jets from the networks of the solar transition region and chromosphere. *Science* **346**(27), 1255711. DOI. ADS.
- Tingay, S.J., Goeke, R., Bowman, J.D., Emrich, D., Ord, S.M., Mitchell, D.A., Morales, M.F., Booler, T., Crosse, B., Wayth, R.B., Lonsdale, C.J., Tremblay, S., Pallot, D., Colegate, T., Wicencac, A., Kudryavtseva, N., Arcus, W., Barnes, D., Bernardi, G., Briggs, F., Burns, S., Bunton, J.D., Cappallo, R.J., Corey, B.E., Deshpande, A., Desouza, L., Gaensler, B.M., Greenhill, L.J., Hall, P.J., Hazelton, B.J., Herne, D., Hewitt, J.N., Johnston-Hollitt, M., Kaplan, D.L., Kasper, J.C., Kincaid, B.B., Koenig, R., Kratzenberg, E., Lynch, M.J., McKinley, B., McWhirter, S.R., Morgan, E., Oberoi, D., Pathikulangara, J., Prabu, T., Remillard, R.A., Rogers, A.E.E., Roshi, A., Salah, J.E., Sault, R.J., Udaya-Shankar, N., Schlagenhauer, F., Srivani, K.S., Stevens, J., Subrahmanyam, R., Waterson, M., Webster, R.L., Whitney, A.R., Williams, A., Williams, C.L., Wyithe, J.S.B.: 2013, The Murchison Widefield Array: The Square Kilometre Array Precursor at Low Radio Frequencies. *PASA* **30**, e007. DOI. ADS.
- Tsuchiya, A.: 1963, Polarization of Storm Bursts of Solar Radio Emission at 200 Mc/s. *Pub. Astron. Soc. Japan* **15**, 368. ADS.
- Tun, S.D., Vourlidas, A.: 2013, Derivation of the Magnetic Field in a Coronal Mass Ejection Core via Multi-frequency Radio Imaging. *Astrophys. J.* **766**, 130. DOI. ADS.
- Vocks, C., Mann, G., Breitling, F., Bisi, M.M., Dąbrowski, B., Fallows, R., Gallagher, P.T., Krankowski, A., Magdalenic, J., Marqué, C., Morosan, D., Rucker, H.: 2018, LOFAR observations of the quiet solar corona. *Astron. Astrophys.* **614**, A54. DOI. ADS.
- Wayth, R.B., Tingay, S.J., Trott, C.M., Emrich, D., Johnston-Hollitt, M., McKinley, B., Gaensler, B.M., Beardsley, A.P., Booler, T., Crosse, B., Franzen, T.M.O., Horsley, L., Kaplan, D.L., Kenney, D., Morales, M.F., Pallot, D., Sleaf, G., Steele, K., Walker, M., Williams, A., Wu, C., Cairns, I.H., Filipovic, M.D., Johnston, S., Murphy, T., Quinn, P., Staveley-Smith, L., Webster, R., Wyithe, J.S.B.: 2018, The Phase II Murchison Widefield Array: Design overview. *Pub. Astron. Soc. Austral.* **35**. DOI. ADS.
- Wentzel, D.G.: 1984, Polarization of fundamental type III radio bursts. *Solar Phys.* **90**, 139. DOI. ADS.
- Wentzel, D.G., Zlobec, P., Messerotti, M.: 1986, A test for large-angle radio scattering in the solar corona. *Astron. Astrophys.* **159**, 40. ADS.
- White, S.M.: 1999, Radio Versus EUV/X-Ray Observations of the Solar Atmosphere. *Solar Phys.* **190**, 309. DOI. ADS.
- White, S.M., Kundu, M.R.: 1997, Radio Observations of Gyroresonance Emission from Coronal Magnetic Fields. *Solar Phys.* **174**, 31. DOI. ADS.
- White, S.M., Thejappa, G., Kundu, M.R.: 1992, Observations of mode coupling in the solar corona and bipolar noise storms. *Solar Phys.* **138**, 163. DOI. ADS.
- Willes, A.J., Melrose, D.B.: 1997, The Polarisation of Second Harmonic Coronal Type III Bursts. *Solar Phys.* **171**, 393. DOI. ADS.
- Willson, R.F.: 2005, Very Large Array and SOHO Observations of Type I Noise Storms, Large-Scale Loops and Magnetic Restructuring in the Corona. *Solar Phys.* **227**, 311. DOI. ADS.
- Zheleznyakov, V.V.: 1970, *Radio emission of the sun and planets*. ADS.
- Zheleznyakov, V.V.: 1977, *Electromagnetic waves in cosmic plasma. Generation and propagation*. ADS.
- Zheleznyakov, V.V., Zlotnik, E.Y.: 1964, Polarization of Radio Waves Passing through a Transverse Magnetic Field Region in the Solar Corona. *Soviet Astron.* **7**, 485. ADS.